Czech Technical University in Prague
Faculty of Nuclear Sciences and Physical Engineering
Department of Physical Electronics

Inverse Compton scattering by laser-accelerated electrons

Diploma thesis

Author: Bc. Tomáš Kerepecký
Supervisor: Ing. Jan Pšikal, Ph.D.
Consultants: Ing. Vojtěch Horný,
Ing. Jaroslav Nejdl, Ph.D.
Academic year: 2016/2017

Před svázáním místo téhle stránky vložíte zadání práce s podpisem děkana (bude to jediný oboustranný list ve Vaší práci) !!!!

Declaration

I declare that I wrote this diploma thesis independently and exclusively with the use of cited bibliography

Prague, ...

Bc. Tomáš Kerepecký

Acknowledgements

First of all, I would like to express my deepest gratitude to my supervisor Ing. Jan Pšikal, Ph.D., and to my consultants Ing. Jaroslav Nejdl, Ph.D. and Ing. Vojtěch Horný for the useful comments, remarks, and engagement through the learning process of this diploma thesis. Furthermore, I would like to thank the whole RP2 team at ELI Beamlines for creating a great work environment. Special thanks to my family and my second family in the church Třináctka. Above all, thanks to the Great Almighty, the author of knowledge and wisdom, for his countless love.

Tomáš Kerepecký

Thesis title:
Inverse Compton scattering by laser-accelerated electrons

Author: Bc. Tomáš Kerepecký

Branch of study: Computational physics
Kind of thesis: Diploma thesis

Supervisor: Ing. Jan Pšikal, Ph.D.

Consultants: Ing. Vojtěch Horný (ÚFP AV ČR),
Ing. Jaroslav Nejdl, Ph.D. (FzÚ AV ČR)

Abstract: This thesis deals with the study of X- and γ-radiation during the interaction of relativistic electrons with the intense electromagnetic field. This mechanism is called inverse Compton scattering. In the first part, underlying physics of electron acceleration in underdense plasma based on the method called laser wakefield acceleration is presented. Furthermore, the thesis focuses on energy upshift of laser photons while interacting with relativistic electrons. The conversion of laser photons to γ-radiation occurs as the double Doppler upshift. An analytic expression of the spectral intensity of radiation is derived and described. For the purpose of examining the properties of radiation from inverse Compton scattering, a new $\mathcal{COCO}$ code has been implemented. Radiation spectrum is computed through the use of fast Fourier transform of the radiation field of electrons. In the practical part of the thesis, the description of the simulations is provided and achieved simulation results are discussed. In all tested cases, simulation results agreed with the theory as well as with corresponding results from the scientific literature. Electron bunch simulation has been performed at ELI ECLIPSE computational cluster. Results show the similarity of the spectral shape as well as the divergence in the case of an electron bunch and a single electron. Algorithm was relatively fast in the case of a single electron simulation, therefore, it could be used as a useful tool during the experiments in the Prague Asterix Laser System facility or in the international project ELI-beamlines.

Key words: Inverse Compton scattering, laser wakefield acceleration, relativistic electrons, gamma radiation, spectral intensity of radiation, Fourier transform.

Název práce:
Inverzní Comptonův rozptyl na laserem urychlených elektronech

Autor: Bc. Tomáš Kerepecký

Obor: Informatická fyzika
Druh práce: Diplomová práce

Vedoucí práce: Ing. Jan Pšikal, Ph.D.

Konzultanti: Ing. Vojtěch Horný (ÚFP AV ČR),
Ing. Jaroslav Nejdl, Ph.D. (FzÚ AV ČR)

Abstrakt: Tato práce se zabývá studiem vzniku rentgenového až gama záření při interakci elektromagnetického záření s relativistickými elektrony. Tento proces se nazývá inverzní Comptonův rozptyl. Úvodní část shrnuje základní poznatky v problematice urychlování elektronů na relativistické rychlosti v podkriticky hustém plazmatu pomocí metody laser wakefield acceleration. Práce dále popisuje využití takto urychlených elektronů ke zvyšování energie rozptýlených fotonů vlivem dvojitého Dopplerova posunu. Je zde odvozen a popsán analytický vztah pro výpočet spektrální intenzity vyzařování elektronu a shrnuty vlastnosti záření. Pro účely zkoumání vlastností záření při inverzním Comptonvě rozptylu byl vyvinut kód $\mathcal{COCO}$, implementovaný v programu Matlab. Výpočet spektralní intenzity vyzařování využívá metody rychlé Fourierovy transformace radiačního pole elektronů. Praktická část práce se zaměřuje na popis simulací navrženého kódu a shrnuje dosažené výsledky. Ve všech testovaných případech se výsledky simulací shodovali s teorií či modelovými případy z dostupné literatury. Simulace elektronového svazku byly prováděny na výpočetním clusteru ELI ECLIPSE. Je zde ukázáno, že tvar spektra či divergence záření jsou podobné pro elektronový svazek i jeden elektron. V případě simulací jednoho elektronu byl navíc algoritmus velmi rychlý a je tak možné ho využít při experimentech v badatelském centru PALS nebo na mezinárodním projektu ELI-beamlines.

Klíčová slova: Inverzní Comptonův rozptyl, urychlování brázdovým polem, relativistické elektrony, gama záření, spektrum intenzity vyzařování, Fourierova transformace.

Contents

List of abbreviations

ICS	inverse Compton scattering
LWFA	laser wakefield acceleration
$\mathcal{COCO}$	"Compton code"
RHS	right-hand side
L frame	laboratory frame of reference
ER frame	electron rest frame of reference
QED	quantum electrodynamics
XUV	extreme ultraviolet
FEL	free-electron laser
FWHM	full width at half maximum
FFT	fast Fourier transform
BW	bandwidth

Fundamental physical constants

m_e	$9.11 \cdot 10^{-31}\,\mathrm{kg}$	electron rest mass
e	$1.60 \cdot 10^{-19}\,\mathrm{C}$	elementary charge
ε_0	$8.85 \cdot 10^{-12}\,\mathrm{F \cdot m^{-1}}$	vacuum permittivity
h	$6.63 \cdot 10^{-34}\,\mathrm{J \cdot s}$	Planck constant
$\hbar$	$1.05 \cdot 10^{-34}\,\mathrm{J \cdot s}$	reduced Planck constant
c	$299792458\,\mathrm{m \cdot s^{-1}}$	speed of light in vacuum

Introduction

During the last decades, the problem of the interaction of relativistic electrons with intense electromagnetic fields has received considerable attention. The scattering of light on high-energy electron beams has become an indispensable tool for generating tunable wide range X- and γ- radiation. These so-called Compton sources based on the physical phenomena called *inverse Compton scattering* have found applications in spectroscopy [1, 2, 3], medicine [4] or ultrafast radiography [5, 6]. The conversion of laser photons to γ-radiation occurs as the double Doppler upshift [7] of the laser frequency while scattering on electrons with high Lorentz γ factor. The maximum energy of scattered photons is approximately given by $4\gamma^2\mathcal{E}_0$ [8], where $\mathcal{E}_0$ is laser photon energy. Therefore, scattering of laser photons from visible range ($\mathcal{E} \sim 1\,\mathrm{eV}$) by ultra-relativistic electrons with $\gamma \sim 100$ can lead to generation of γ-photons with energies in the order of 100 keV.

Electrons with high Lorentz factor γ can be obtained by accelerating them up to velocities close to the speed of light. All optical Compton sources [9, 10] uses electrons accelerated in plasma. Up to date, the most promising method seems to be the *laser wakefield acceleration* (LWFA) [11, 12, 13, 14], where electrons are trapped in the wakefield dragged by the laser pulse and accelerated to GeV energy in a distance of only a few centimeters [15].

A large number of publication has been devoted to the theory of scattering of intense laser radiation by free electrons [16, 17, 18, 19], however, a quantitative analytical description of the inverse Compton scattering still remains an open question. Therefore, the numerical computation of inverse Compton scattering and in general radiation emission from accelerated electrons has been addressed by several authors. A variety of methods has been proposed: analytic [19], semianalytic [20, 21] or Monte Carlo [22, 23].

In this thesis, properties of the inverse Compton scattered radiation, such as spectrum, divergence and the number of emitted photons is investigated by calculation of the Liénard-Wiechert potentials directly from electron trajectories. New and relatively fast *Compton code* ($\mathcal{COCO}$) has been implemented by the author in the program Matlab. The equations of motion of electrons in the laser field are numerically calculated in order to obtain trajectories of electrons. From the trajectories, radiation fields are computed at the position of the observer. In order to save computer memory and as well as to keep coherence properties in resulting radiation, radiated fields from each electron are first summed and then the spectrum is computed using fast Fourier transform.

The thesis is organized as follows. The first chapter is devoted to the laser wakefield acceleration. The review of the most important physical phenomena necessary for electron acceleration in plasma is presented here. At the end of this chapter, electron injection schemes and recent progress in LWFA experiments are discussed. The second chapter is focused on the theory of photon-electron interaction. At the beginning of this chapter, ordinary Compton and Thomson scattering are introduced. Then, photon energy upshift due to the inverse Compton scattering is described. In the third chapter, the general formalism of radiation from an accelerated relativistic electron is presented. The review of the synchrotron light sources is also provided in this chapter. At the end of the third chapter, the relevant properties of the scattered radiation are summarized. The fourth chapter describes the $\mathcal{COCO}$ simulation of ICS. In the first part, an algorithm for computing electron trajectory, calculation of radiation field and radiation spectra is presented. In the second part, calculation of ICS spectra and radiation properties using $\mathcal{COCO}$ are discussed for the single electron as well as for an electron bunch. At the end, the thesis results are summarized and conclusions are deduced.

Chapter 1

Laser Wakefield Acceleration

The mechanism of electron acceleration in laser-produced plasma was first proposed by Tajima and Dawson [24]. They showed that strong laser fields are capable to create large amplitude waves in plasmas due to the non-linear ponderomotive force [25]. Electrons injected into this so called plasma waves could be accelerated due to the intense electric field of a plasma waves up to energies of order GeV [26]. The main advantage of plasmas relies on their ability to sustain up to four orders magnitude larger accelerating gradient (100 GeV/m) than a conventional accelerators [11]. This opens the possibility to accelerate electrons up to 1 GeV in centimeter-scale plasmas [27]. The most promising method commonly used for electron acceleration in plasma is called *laser wakefield acceleration* (LWFA) [11, 12, 13, 14, 28]. The principle of this method is briefly summarized in this chapter.

1.1 Ultrashort intense laser pulses

One of the greatest breakthroughs in the history of laser technology was proposing two methods: *mode-locking* and *chirp pulse amplification*. Former led to a generation of ultra-short laser pulses, latter allowed amplification of these pulses up to PW power [17].

In comparison with other light sources, radiation generated by laser is considered to be monochromatic and coherent. However, in all practical cases, the laser light is not truly monochromatic. Light that passes through the gain medium is amplified by way of stimulated emission, nevertheless energy levels in atoms are broaden due to various physical phenomena, thus outgoing radiation is not strictly monochromatic but is centered around a central wavelength in a narrow spectral band called *laser gain bandwidth* (Fig. 1.1a).

The gain medium is surrounded by optical cavity (or optical resonator) which is an arrangement of two mirrors on either end of the gain medium. In the cavity, due to constructive and destructive interference, only standing longitudinal waves (cavity modes) are generated (Fig. 1.1b). The allowed modes of the cavity are those where the mirror separation distance L is equal to an exact multiple of half the

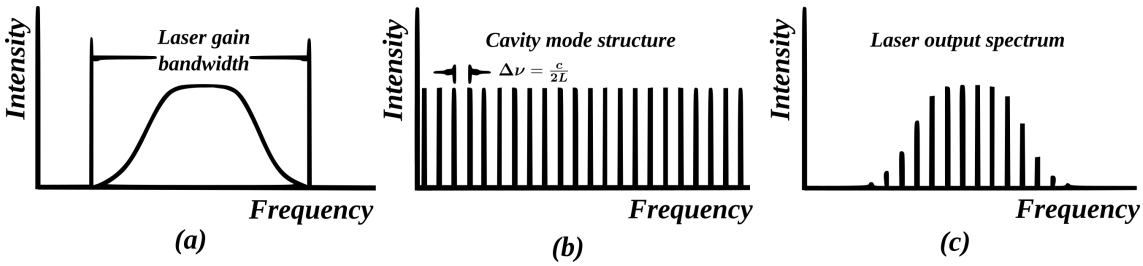

Figure 1.1: (a) Laser gain bandwidth of radiation emitted in gain medium of laser. (b) Longitudinal cavity modes generated in resonator. (c) Resulting laser cavity modes when a gain bandwidth of a laser amplifier is combined with resonances of a two-mirror laser cavity.

wavelength λ, $L = q \cdot \lambda/2$, where $q \in \mathbb{N}$ [29]. Resulting laser output spectrum consists of those cavity modes which are also in the laser gain bandwidth (Fig. 1.1c).

The phases of outgoing modes are random, therefore there is a significant loss of energy due to destructive interference. In order to receive maximum intensity of output radiation, fixed-phase relationship between longitudinal modes of the laser's resonant cavity must be induced. This is the basis of the technique called *mode-locking* [30], which allows one to produce pulses with extremely short pulse duration, of the order of 10^{-12} s and even shorter.

Further amplification of these intense pulses may cause damage of amplifiers and other optical elements. To some extent this problem has been overcome by *chirped pulse amplification* method [31]. The principle is follows: generated short pulse with a low energy, made up by different frequencies is initially stretched out in time, then amplified and finally recompressed back to original pulse width. For stretching pulses, the pair of diffraction gratings with positive dispersion may be used (Fig. 1.2a). It is arranged so that the low-frequency component (red color) of the laser pulse travels a shorter path than the high-frequency component (blue color) does. As a result, the stretched pulse has longer pulse duration (hence lower intensity) than the original one by a factor of 10^3 to 10^5. Therefore, this low-intensity laser pulse may be safely introduced to the gain medium and amplified by a factor of 10^6 or more. Eventually second pair of gratings reverses the dispersion of the stretcher, and recompresses the pulse back to original pulse duration (Fig. 1.2b).

The method of *chirped-pulse amplification* has allowed the construction of lasers with intensities of the order of 10^{22} $\mathrm{W \cdot cm^{-2}}$. Such lasers can be used for *laser wakefield acceleration* enabling electrons to be accelerated in plasma to relativistic energies of the order of GeV.

New generation of 10 PW lasers, such as ELI [32], VULCAN [33] and APOLLON [34] is expected to manage intensities in order of 10^{23} $\mathrm{W \cdot cm^{-2}}$. In the regions with such a high electric field, matter is almost instantly ionized and electrons can be accelerated to ultra-relativistic energies. Electric field observable in the rest frame of the counterpropagating ultra-relativistic electrons to the laser beam can reach the strength relatively close to the Schwinger limit of quantum electrodynamics (QED) $E_s = 1.3 \cdot 10^{18}$ $\mathrm{V \cdot m^{-1}}$ [35], therefore processes such as pair production, radiation reaction or the inverse Compton scattering become even more significant.

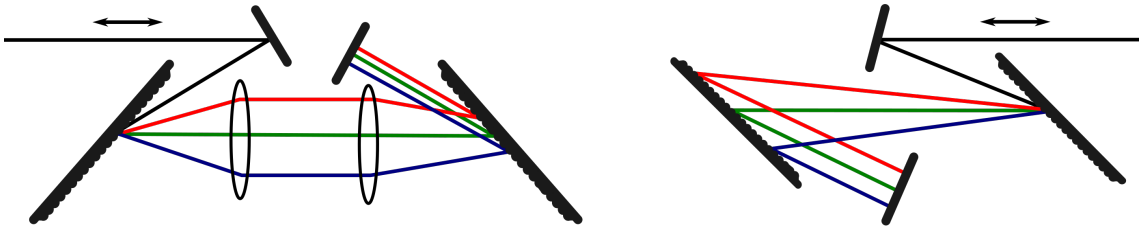

Figure 1.2: Chipred pulse amplification. Left: laser pulse stretching using the pair of diffraction gratings with positive dispersion. Right: laser pulse compression using the pair of diffraction grating with negative dispersion.

Instead of laser intensity it is convenient to use a *laser strength parameter* defined as $a_0 = eA_0/m_e c^2$, where A_0 is vector potential amplitude, e and m_e electron charge and rest mass respectively and c is the speed of light in vacuum. Relation between the laser intensity I and the laser strength parameter is given in practical units by:

$$a_0 \simeq 0.85 \cdot 10^{-9} \lambda[\mu\text{m}] \sqrt{I[\text{W} \cdot \text{cm}^{-2}]}, \tag{1.1}$$

where λ is the laser wavelength. Table 1.1 shows typical values of a_0, corresponding values of laser intensity and the type of the plasma created after laser-matter interaction.

a_0	Intensity $[\text{W} \cdot \text{cm}^{-2}]$	Type of plasma
0.1	$2.16 \cdot 10^{16}$	ionized gas
1	$2.16 \cdot 10^{18}$	plasma
100	$2.16 \cdot 10^{22}$	relativistic plasma
1000	$2.16 \cdot 10^{24}$	QED plasma

Table 1.1: Dependence of laser intensity with the wavelength $\lambda = 800$ nm on the laser strength parameter a_0 and the corresponding type of the plasma created after laser-matter interaction.

1.2 Plasma

Plasma is one of the four fundamental states of matter and also the most abundant form of ordinary matter in the universe. It can be defined as a quasi-neutral ionized gas containing enough free charges to make collective electromagnetic effects important for its physical behavior [36]. Particles in a plasma interact not only by collisions but also by the long range Coulomb force. This means that each plasma particle interacts with a large number of other particles. Plasma is conductive and reacts strongly to external electric and magnetic fields. The quasi-neutrality of a plasma means that the densities of negative and positive charges are almost equal, while at smaller scales charges making up the plasma may give rise to charged regions and electric fields. Since electrons are lighter than ions, they are very mobile and oscillate in plasma with the plasma frequency

$$\omega_p = \sqrt{\frac{n_e e^2}{m_e \varepsilon_0}}, \tag{1.2}$$

where n_e, m_e, e is the electron density, rest mass and charge respectively and ε_0 is the vacuum permittivity. The plasma frequency is a typical plasma parameter which modifies the dispersion relation of electromagnetic wave going through plasma as follows:

$$\omega_0^2 = \omega_p^2 + c^2 k^2, \tag{1.3}$$

where ω_0 is the frequency of electromagnetic wave and k the wave number. Laser (electromagnetic wave) can propagate through a plasma only if the wave number k is real, in other words $\omega_0 > \omega_p$. From the equation $\omega_0 = \omega_p$ one can obtain the *critical plasma density*

$$n_c = \frac{\omega_0^2 m_e \varepsilon_0}{e^2}, \tag{1.4}$$

which determines the threshold for a laser propagation through a plasma. For example, the critical density for the Ti:Sapphire laser (wavelength of $\lambda = 800\,\mathrm{nm}$) is $1.75 \cdot 10^{21}\,\mathrm{cm}^{-3}$.

If the electron density is smaller than the critical density ($n_e < n_c$), the wave number in equation (1.3) is real and the laser beam can propagate through a plasma. Such plasma is called *underdense*. Otherwise, if the critical density is exceeded, the plasma is called *overdense* and a laser is reflected from the plasma. Since the laser propagation is essential for an electron acceleration in plasma, the laser wakefield acceleration is only possible in underdense plasma.

1.3 Laser ionization

Ionization, which is necessary for the plasma formation, is the process by which an atom or a molecule acquires a negative or positive charge by gaining or losing electrons to form ions. One can define the degree of ionization

$$\alpha = \frac{n_e}{n_i + n_0}, \tag{1.5}$$

where n_e, n_i and n_0 are densities of electrons, ions and neutrons respectively. Even a partially ionized gas in which as little as 1 % of the particles are ionized can have the characteristics of a plasma [37]. Atoms may be ionized by the interaction with intense laser pulses. The electron bound to an atom can absorb incoming photons of the laser and thus move to higher energy levels. If the number of photons is sufficiently high, the electron can get enough energy to leave the Coulomb potential well and leave the atom. This process which is called *multiphoton ionization* [38] is depicted in Fig. 1.3a, where $\mathcal{E}_i$ is the ionization energy and $\mathcal{E}_k$ is the kinetic energy of an outgoing electron given by

$$\mathcal{E}_k = n_{min}\mathcal{E}_{ph} - |\mathcal{E}_i|\,, \tag{1.6}$$

where n_{min} is the minimum number of photons with the energy $\mathcal{E}_{ph}$ satisfying inequality $n_{min}\mathcal{E}_{ph} > |\mathcal{E}_i|$. For the $n > n_{min}$, the energy of extra photons contributes to the resulting kinetic energy of the leaving electron. Then it is rather called *above threshold ionization* [39]. This is illustrated in Fig. 1.3b. For example to ionize hydrogen atom with ionization energy $\mathcal{E}_k = 13.6\,\text{eV}$, electron has to absorb at least nine photons of Ti:Sapphire laser, where each of these photons has the energy $\mathcal{E}_{ph} \simeq 1.6\,\text{eV}$.

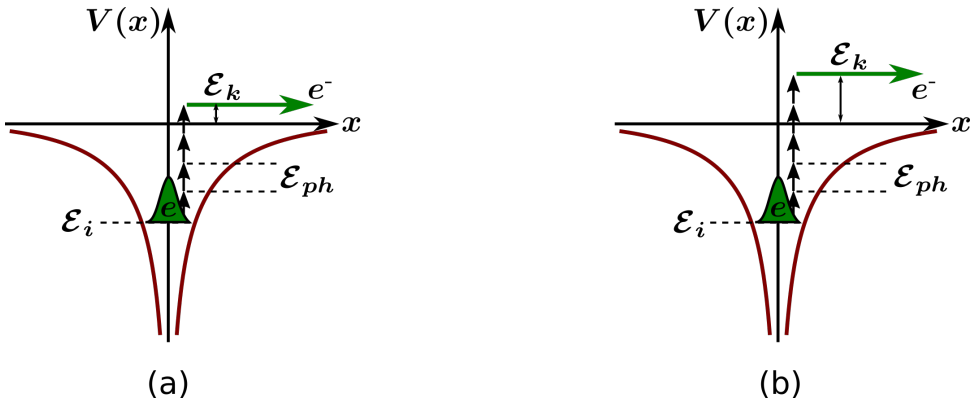

Figure 1.3: Schematic illustration: (a) multiphoton ionization, (b) above threshold ionisation.

Increasing the laser intensity to the order of $10^{14} - 10^{15}\,\text{W}\cdot\text{cm}^{-2}$ ($a_0 \simeq 0.01$) leads to a laser field comparable to the Coulomb field in the atom. In this case, which is illustrated in Fig. 1.4a, potential barrier is deformed. The barrier divides a space into two regions where the electron is bound or free. A local maximum of the barrier is called the *saddle point*. The electron can leave the atom by tunnelling through the potential barrier. This is called *tunelling ionization* [40].

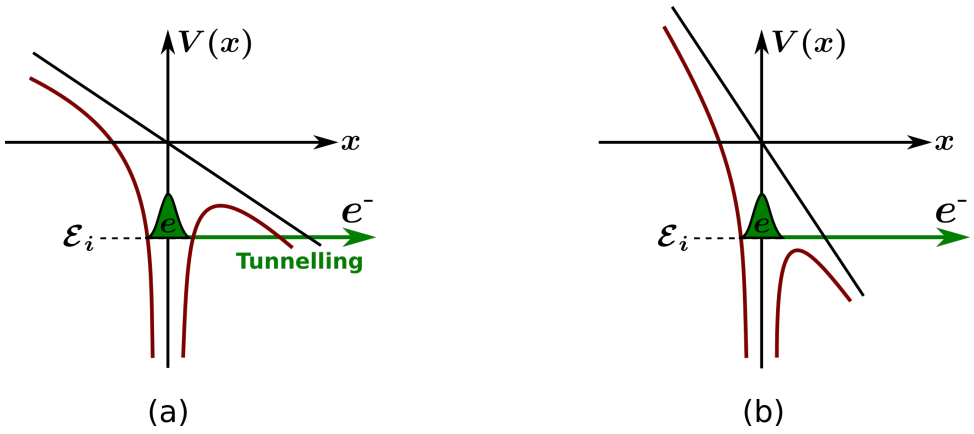

Figure 1.4: Schematic illustration: (a) tunnelling ionisation; (b) barrier-suppression ionization.

Laser field with the intensity of the order $10^{15}\,\mathrm{W}\cdot\mathrm{cm}^{-2}$ ($a_0 \gtrsim 0.02$) and higher can completely deform Coulomb potential as it is shown in Fig. 1.4b. The energy of ground state of the atom is above the potential well, thus electron is no longer bounded to the atom and may be directly released. This process, which is called *barrier-suppression ionization* dominates for ultra intense laser pulses.

1.4 Ponderomotive force

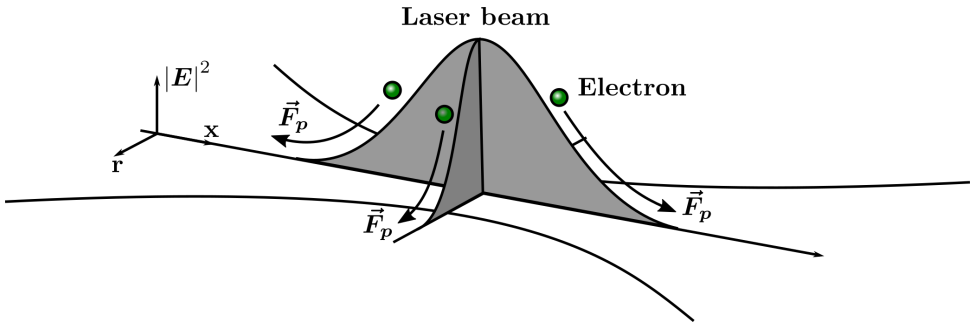

Figure 1.5: Ponderomotive force: laser intensity $I \sim |E|^2$ versus propagation (x) and radial (r) direction. Ponderomotive force $\boldsymbol{F}_p$ pushes electrons out of the high-intensity region.

When the laser propagates through a plasma the nonlinear ponderomotive force of the laser pushes particles in the direction opposite to the gradient of the laser intensity $I \sim |E|^2$ according to the equation [25]

$$\boldsymbol{F}_p = -\frac{q^2}{4m\omega}\nabla|E|^2\,, \tag{1.7}$$

where q and m is the charge and the mass of the particle respectively, ω is the angular frequency of the laser, and E is the amplitude of the electric field. Ponderomotive force is inversely proportional to the particle mass, thus electrons are influenced much more than heavy ions. Scheme of this process is depicted in Fig. 1.5.

1.5 Plasma waves and bubble regime

Strong laser pulse propagating through a plasma is again considered. Ponderomotive force of the laser pushes electrons out of the high-intensity region, while ions are relatively inert due to their higher mass. This creates a spatial charge separation. Induced electric field attracts ejected electrons back to their initial positions. However, due to the inertia, electrons overcome their initial positions and begin to oscillate. This introduces a longitudinal variation in charge density, so-called plasma waves (or *Langmuir waves*) which travel with the group velocity of the laser pulse behind the laser pulse.

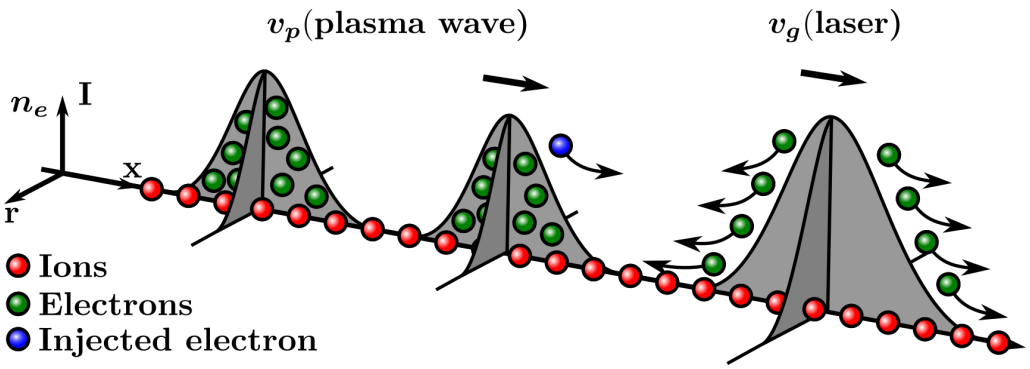

Figure 1.6: Laser intensity I (peak on the right) and plasma density n_e (two peaks on the left) versus propagation (x) and radial (r) direction. Longitudinal plasma wave arises in the wake of the intense laser pulse. Electron, which is trapped into the plasma wave (blue ball), can be therefore accelerated.

Electrons can be injected into plasma waves, as it is shown in Fig. 1.6 and eventually accelerated in the wakefield dragged by the laser pulse. This is the reason why the method is called *laser wakefield acceleration*. Up to date, the most efficient mechanism using this method is called the *bubble regime* (cavitated wakefield regime) [41] where the wake behind the laser consists of an ion cavity (bubble) having a spherical shape. In order to reach this regime, three conditions must be fulfilled. First and the most important, the laser strength parameter must be sufficiently high ($a_0 > 2$) to expel most of the electrons out of the focal spot. Second, in order to reach a spherical shape of an ion cavity, waist w_0 of the focused laser pulse has to satisfy equation [11]

$$k_p w_0 = 2\sqrt{a_0}, \tag{1.8}$$

where $k_p = \omega_p/c$ is a plasma wavenumber and a_0 is the laser strength parameter. Third, laser pulse duration must be of the order of half a plasma wavelength ($c\tau \sim \lambda_p/2$). Electrons can be trapped at the back of the cavity and accelerated by the high electric field (the space-charge force) until they reach the middle of the cavity where they start to decelerate. The distance over which electrons must propagate before they reach that point is called the *dephasing length*. It is much larger than the bubble radius, as electrons travel almost at the same speed as the wave phase velocity [11]. To be able to use this scheme, some electrons have to be trapped into the ion cavity behind the laser. Therefore, electron injection methods will be summarized in the following section.

1.6 Electron injection

Electron injection into the plasma wave cavity has to be achieved, in order to accelerate electrons by laser wakefield acceleration. The plasma electrons have to gain a sufficient initial momentum to dephase from their fluid motion in the plasma and to be trapped in the bubble behind the laser. This can happen, for example, when the longitudinal plasma wave brakes. This process is called self-injection [42] and due to its simple mechanism is widely used. On the other hand, the self-injection occurs in the random phase of the plasma wave and thus is difficult to control. Several different injection schemes such as optical [43] or ionization [44] injection were proposed.

1.6.1 Self-injection

Self-injection is the most common way of plasma electron injection. If the plasma wave amplitude is high enough, many electrons are dephased from the fluid motion trajectories. When the velocity of plasma electrons is equal or higher than the phase velocity of the plasma wave, the wave structure cannot be preserved anymore and so-called wave breaking occurs. Some of these dephased electrons can be trapped by the plasma wave electric field and subsequently accelerated. Electrons are often injected into the plasma wave in different locations and times; thus, it results in an electron beam with a high relative energy spread. The major advantage of this scheme is the fact that there is no need for an accurate spatial and temporal synchronization [42, 45, 46].

1.6.2 Density down-ramp injection

The electron self-injection can be controlled on the sharp density down-ramp serving for forcing the wave breaking in a well defined location of the density gradient. In the experiment density gradient can be achieved using two separate nozzles to supply the gas in the interaction region [47, 48].

1.6.3 Ionization injection

In this scheme a mixture of two gases is used with a small amount of heavier atoms (N, O, Ar). Whereas the plasma originates from the ionization of a light gas (e.g. He) and L-shell electrons of the heavier gas, accelerated electrons are injected by the tunnel ionization of K-shell electrons which occurs close to the laser pulse intensity peak. Since the ionization injection takes place close to the maximum laser intensity region, the electron beam injection is well localized in the time and space [49, 42, 50, 51].

1.6.4 Optical injection

Electron injection can be also triggered by a second laser pulse. Injection pulse has usually lower intensity and propagates against the main laser pulse exciting the wakefield. The pondermotive force of the injection pulse can perturb plasma electron trajectories and deflect them from fluid plasma oscillations. Thus, these electrons can be sufficiently preaccelerated and captured by the wakefield and eventually accelerated. A very strong injection pulse can destroy the wakefield completely and can introduce an instability into electron acceleration [43, 42, 52].

1.7 Relativistic electrons

Electrons trapped into the ion cavity (bubble) behind the laser can be accelerated up to relativistic velocities. However, the term *relativistic* has no exact definition, one can say that Newtonian mechanics fails at velocities greater than $0.1c$, where c is speed of light. At velocities comparable to the speed of light effects of the theory of relativity must be taken into account [53].

Relativistic electrons are usually described by the Lorentz factor γ, the ratio of the total electron energy to the rest electron energy $m_e c^2$ (511 keV). The Lorentz factor γ and the electron velocity v may be calculated from the energy $\mathcal{E}$ of an electron according to the following equations:

$$\gamma = \frac{\mathcal{E}}{m_e c^2}, \tag{1.9}$$

$$v = c\sqrt{1 - \frac{m_e^2 c^4}{\mathcal{E}^2}}, \tag{1.10}$$

where m_e is the electron rest mass and c the speed of light. Table 1.2 shows some values of the electron total energy and corresponding values of the Lorentz factor γ and the electron velocity v.

Electron total energy $\mathcal{E}$ [MeV]	Lorentz factor γ	Electron velocity v [c]
0.511	1.000	0
0.514	1.005	0.10000
5.110	10	0.99869
511.000	1000	0.99999

Table 1.2: Total energy of an electron and corresponding values of Lorentz factor γ and electron velocity v.

1.8 Progress in LWFA experiments

The purpose of this section is to provide an overview of recent experimental progress in laser wakefield acceleration. First, the results from the proceedings of the CAS-CERN Accelerator School 2015 [54] is used to show the progress in the maximum beam energy in laser wakefield accelerator experiments during 2004–2014. This paper uses data set of 52 experiments around the world and shows trends concerning the relationship between plasma density, accelerator length, laser power and the final electron beam energy. Second, recent LWFA experiments and currently attainable parameters of accelerated electron beams from LWFA are summarized.

1.8.1 LWFA from 2004 to 2014

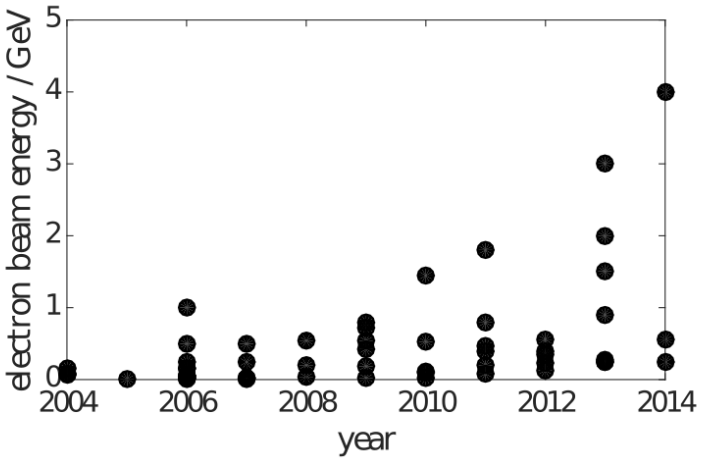

Figure 1.7: Reported maximum electron beam energies from laser wakefield experiments at various laboratories from 2004–2014. Reprinted from [54].

Although LWFA method was proposed in 1979 by Tajima and Dawson [24], the breakthrough in the field of laser-plasma acceleration came in early 2000s, when high power femtosecond laser pulses, using Ti:Sapphire laser systems, became available. In 2002, 200 MeV maximum energy beam was reported by Malka et al. [55]. Since that time, the progress in the maximum beam energy in LWFA experiments has been rapid, as shown in Fig. 1.7. Over one decade electron beam energy increased by a factor of 20 to the current record of 4.2 GeV from the group at the Lawrence Berkeley National Laboratory [26] achieved in 2014. This huge rise of the electron energy is partially due to the fast development of the laser technology. This trend is evident from the Fig. 1.8, where clearly higher-power lasers are capable of producing higher-energy electron beams. This graph also shows dependence of injection mechanisms on the electron beam energy. According to the results, ionization injection experiments produced higher electron beam energies. The same data set also shows (see Fig. 1.9) that the beam energy is directly proportional to the accelerator length and inversely proportional to the electron plasma density. Thus, to keep pushing the electron energy to ever higher values requires operation at lower densities and over longer distances, and such experiments will need more powerful lasers [54].

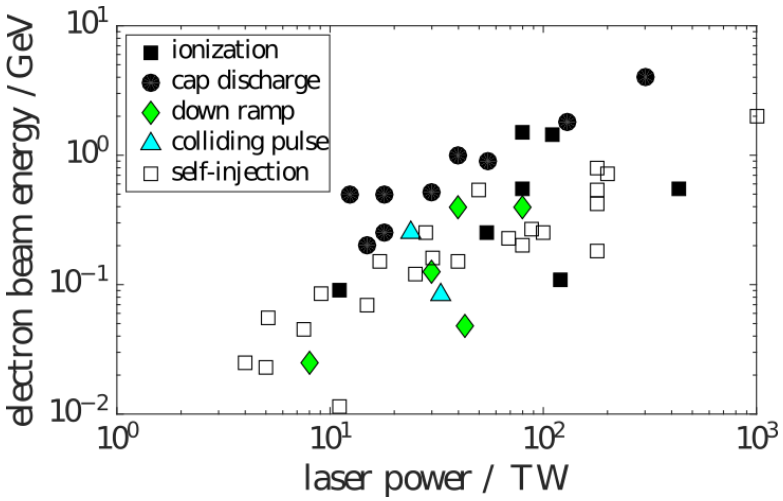

Figure 1.8: Reported maximum electron beam energies from LWFA experiments as a function of laser power at various laboratories from 2004–2014. Symbols distinguish different injection mechanisms used for LWFA. Filled black circles, capillary discharge experiments; black squares, ionization injection; green diamonds, density down-ramp injection; cyan triangles, colliding pulse injection; open black squares, self-injection. Reprinted from [54].

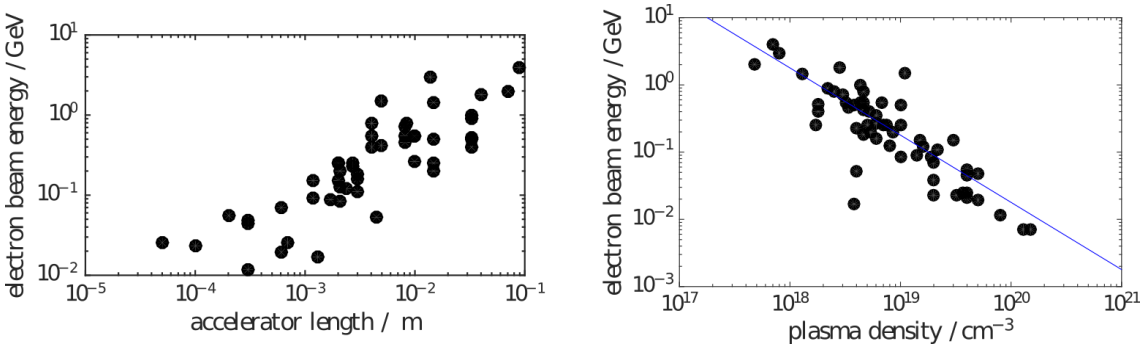

Figure 1.9: Variation of reported electron beam energy with (a) accelerator length, (b) the density in the accelerator. The line shows the relation n_c/n_e, where n_c and n_e are the critical density and the electron plasma density, respectively. Reprinted from [54].

1.8.2 Recent LWFA experiments

The significant growth of the electron beam energy, depicted in Fig. 1.7 stopped in 2014 and up to date the highest electron beam energy in laser wakefield accelerators remains at the value 4.2 GeV achieved by Leemans et al. [26] in Lawrence Berkeley National Laboratory in California. This multi-GeV electron beams with 6% rms energy spread, 6 pC charge, and 0.3 mrad rms divergence have been produced in self-injection regime from a 9-cm-long capillary discharge waveguide with a plasma density of $n_e \simeq 7 \cdot 10^{17}\,\mathrm{cm}^{-3}$, powered by laser pulses with peak power up to 0.3 PW. In the same lab more stable beams with energy $2.7\,\mathrm{GeV} \pm 0.1\,\mathrm{GeV}$ and charge 150 pC were reported by Gonsalves et al. [56] in 2015.

In 2013, one year before the experiment by Leemans et al. was published [26], Wang et al. presented the first experimental demonstration of self-injected, quasi-monoenergetic laser-plasma accelerator of electrons without taking advantage of preformed plasma channels and structured gas cells [27, 57]. Electron bunches with a spectrum peaked at 2 GeV with only few per cent energy spread and sub-miliradian divergence were produced using the Texas Petawatt Laser with a full capacity of

1.1 PW. In this experiment, a simple target consisting of uniform undopted He gas was used and no specialized injection techniques were implemented. Thus, results obtained from this experiment provided a benchmark against which other multi-GeV laser-plasma accelerators can be compared.

However, experimental studies have shown that the self-injection process is highly nonlinear and uncontrollable as it requires large laser strength parameter a_0, to trigger the injection in single low-Z gas plasma [58]. Recently, an electron injection scheme based on ionization (Sec. 1.6.3) was proposed in order to reduce the laser intensity threshold for electron trapping. Nevertheless, ionization-induced electron injection in laser wakefield accelerators has the drawback of generating electron beams with large and continuous energy spreads, severely limiting their future applications. In order to overcome the continuous injection of electrons, a two-stage accelerating configuration was proposed [49] as the way to achieve small energy spread electron beams by ionization injection. Recently single-stage, self-truncated ionization-injection LWFA was proposed [59] and used for the generation of electron beams with peak energy near 500 MeV and a few percent energy spread [58].

In 2016, there were several other ionization-injection LWFA experiments. For example Ti:Sapphire HERCULES laser facility at the university of Michigan investigated the influence of the driver pulse on electron injection process [60]. First experiment considering both LWFA and direct laser acceleration was shown by Shaw et al. [61]. Furthermore, 200-600 MeV electron beams with $0.4\% - 1.2\%$ rms energy spread, 10-80 pC charge, and ~ 0.2 mrad rms divergence was delivered by a new cascaded acceleration scheme by Wang et al. [62]. Finally, some methods based on density tampering were also proposed for the increasing of the electron beam energy gain [63, 64].

Regarding LWFA experiments in the Czech Republic, the possibility to accelerate electrons in a small laboratory equipped with an affordable femtosecond few-terawatt laser system was investigated at Prague Asterix Laser System (PALS) in 2016 by Bohacek et al [65]. Experiment also proved, that the dry air could be an efficient option to create a stable electron source. Electron bunches were produced in dry air with the mean energy of (17.4 ± 1.1) MeV by using 7 TW Ti:sapphire laser system. Electron acceleration in plasma will be also covered in the research project HELL (High-energy electrons by lasers) [66] at ELI Beamlines in Dolní Břežany near Prague.

Chapter 2

Inverse Compton scattering

2.1 Photon energy loss due to photon-electron interaction

In this section, photon-electron interactions when electrons get energy from photons are discussed. After photon interacting with the matter, three fundamental physical phenomena could be distinguished according to the energy of incident photon [67]:

1. **Photoelectric effect**
   The low energy X-ray photon ($\mathcal{E}_{ph} \ll 511\,\mathrm{keV}$) interacts with the matter and after its absorption the electron, which is bound to the inner-shell of an atom, is released. The kinetic energy $\mathcal{E}_k$ of this electron corresponds to difference of the incident photon energy $\mathcal{E}_{ph}$ and the binding energy of the electron $\mathcal{E}_B$, i.e. ($\mathcal{E}_k = \mathcal{E}_{ph} - \mathcal{E}_B$). Vacancy in the inner-shell is afterwards filled by the electron in outer-shell by the process of deexcitation. This is accompanied by either the emission of an electron from the same atom (Auger effect) or emitting characteristic X-ray with an energy equivalent to the energy difference between the corresponding higher and lower state.

2. **Compton Scattering**
   The photon whose energy is comparable to the rest energy of an electron ($\mathcal{E}_{ph} \sim 511\,\mathrm{keV}$) release the electron bound to an atom immediately after hitting the matter. Consequently the photon interacts with the free ejected electron. The part of the photon energy is transformed into the electron and the photon is deflected from its original trajectory. The principle of this mechanism is important for the inverse Compton scattering, therefore, it is described in detail in the Sec. 2.1.1.

3. **Pair production**
   Electron-positron pair production can occur when energy of incident photon exceeds double of the electron rest energy ($\mathcal{E}_{ph} > 1.02\,\mathrm{MeV}$). In this process, whole energy of the photon is converted into mass. Two elementary particles, electron and positron are formed. The lifetime of the positrons is very short. When positron annihilates two photons with an energy of 511 keV are released.

2.1.1 Compton scattering

Compton scattering is a physical phenomenon, when a high energy photon is scattered by an electron initially at rest, and the photon energy is partially transferred to the electron. This inelastic scattering becomes significant once the incident photon energy is comparable to the rest energy of an electron ($\mathcal{E}_0 \sim m_e c^2$). During the scattering, the photon loses part of its energy and thus well known Compton shift of the wavelength occurs. This process also gave clear and independent evidence of particle-like behavior of the light. Arthur Holly Compton [68] observed this phenomenon in the 20s of the 19th century and for its discovery was awarded by the Nobel Prize in 1927.

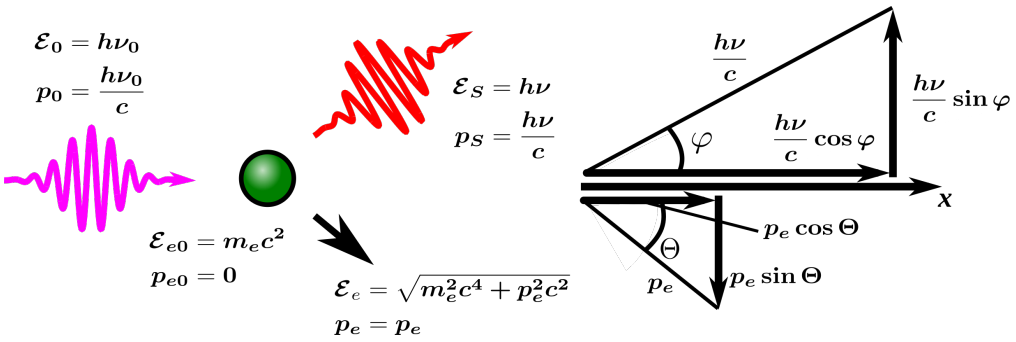

Figure 2.1: Compton scattering scheme. The photon with the energy $\mathcal{E}_0 = h\nu_0$ and the momentum $p_0 = h\nu_0/c$ propagates along the x-axis and hits the electron at rest with the energy $\mathcal{E}_{e0} = m_e c^2$ and the momentum $p_{e0} = 0$. After an interaction, the electron is scattered at the angle Θ from the x axis and travels with the momentum p_e and the energy $\mathcal{E}_e$. The photon is scattered at the angle φ from the x axis and has the shifted energy $\mathcal{E}_S = h\nu$ and momentum $p_S = h\nu/c$. h is the Planck constant and ν_0 (resp. ν) denotes the incident photon frequency (resp. scattered photon frequency).

Compton scattering process is depicted in Fig. 2.1. It will be used for obtaining the Compton shift equation. All quantities used in the following equations (2.1)-(2.3) are given in the description of Fig. 2.1. According to the laws of conservation, equations for longitudinal and transverse momentum can be written as

$$\begin{aligned} \frac{h\nu_0}{c} + 0 &= \frac{h\nu}{c}\cos\varphi + p_e\cos\Theta, \\ 0 &= \frac{h\nu}{c}\sin\varphi - p_e\sin\Theta, \end{aligned} \tag{2.1}$$

and the conservation energy equation reads

$$h\nu_0 + m_e c^2 = \sqrt{m_e^2 c^4 + p_e^2 c^2} + h\nu. \tag{2.2}$$

The combination of these equations gives well known Compton shift equation

$$(\lambda - \lambda_0) = \lambda_c(1 - \cos\varphi), \tag{2.3}$$

where $\lambda_c = \frac{h}{m_e c}$ defines Compton wavelength.

According to the equation (2.3) the change of wavelength depends only on the angle φ between the direction of incident and scattered photon. The greatest change occurs when $\varphi = 180°$, therefore $\lambda - \lambda_0 = 2\lambda_c$. Also, the heavier particle is considered, the

smaller Compton wavelength and thus smaller shift. For an electron the Compton wavelength is $\lambda_c = 2.43\,\text{pm}$. Maximum wavelength shift is then $\Delta\lambda = 4.86\,\text{pm}$. For inelastic electron-photon scattering when $\varphi \neq 0$, there is always Compton shift of the wavelength and photon gives a portion (sometimes negligible) of its energy to an electron.

2.1.2 Thomson scattering

Thomson scattering is the elastic scattering of the photon by the free electron at rest when the photon energy does not change. More precisely, if the energy of the incident photon $\mathcal{E}_0$ is much smaller than the electron rest energy ($\mathcal{E}_0 \ll m_e c^2$), the photon wavelength is much greater than the Compton wavelength. Regarding equation (2.3) Compton shift is then negligible.

Using the relation between wavelength and energy of photon $\mathcal{E} = hc/\lambda$, the equation (2.3) may be rewritten in the form of energy as

$$\mathcal{E}_S = \frac{\mathcal{E}_0}{1 + \frac{\mathcal{E}_0}{m_e c^2}(1 - \cos\varphi)}, \tag{2.4}$$

where $\mathcal{E}_0$ and $\mathcal{E}_S$ is the energy of incident and scattered photon respectively. Furthermore, considering maximum Compton shift (backscattering with $\varphi = 180°$), equation (2.4) simplifies to:

$$\mathcal{E}_S = \frac{\mathcal{E}_0}{1 + \frac{2\mathcal{E}_0}{m_e c^2}}. \tag{2.5}$$

Equation (2.5) helps to understand the importance of the Compton shift and to quantitatively distinguish between the Compton and Thomson scattering. Table 2.1 summarizes results for different types of electromagnetic radiation. For visible up to extreme ultraviolet (XUV) radiation, the Compton shift is negligible. When photon reaches X-ray regime, the energy transferred from the incident photon to the electron becomes more significant. Backscattered γ photon loses almost all of its energy, however, the probability of such interaction is very low.

Radiation	Energy $\mathcal{E}_0$	Energy $\mathcal{E}_S$	Energy transferred
Visible	2.55 eV	2.55 eV	0 %
XUV	511 eV	510 eV	0.2 %
Soft X-rays	5.11 keV	5.01 keV	2 %
Hard X-rays	511 keV	170 keV	67%
Gamma rays	5.11 MeV	0.24 MeV	95%

Table 2.1: Compton shift of photon energy for different types of electromagnetic radiation when photon is scattered back to the opposite direction with regard to the direction of incident photon ($\varphi = 180°$). $\mathcal{E}_0$ and $\mathcal{E}_S$ is the energy of incident and scattered photon respectively. Last column denotes the maximum energy transferred for a given configuration.

2.2 Photon energy gain due to photon-electron interaction

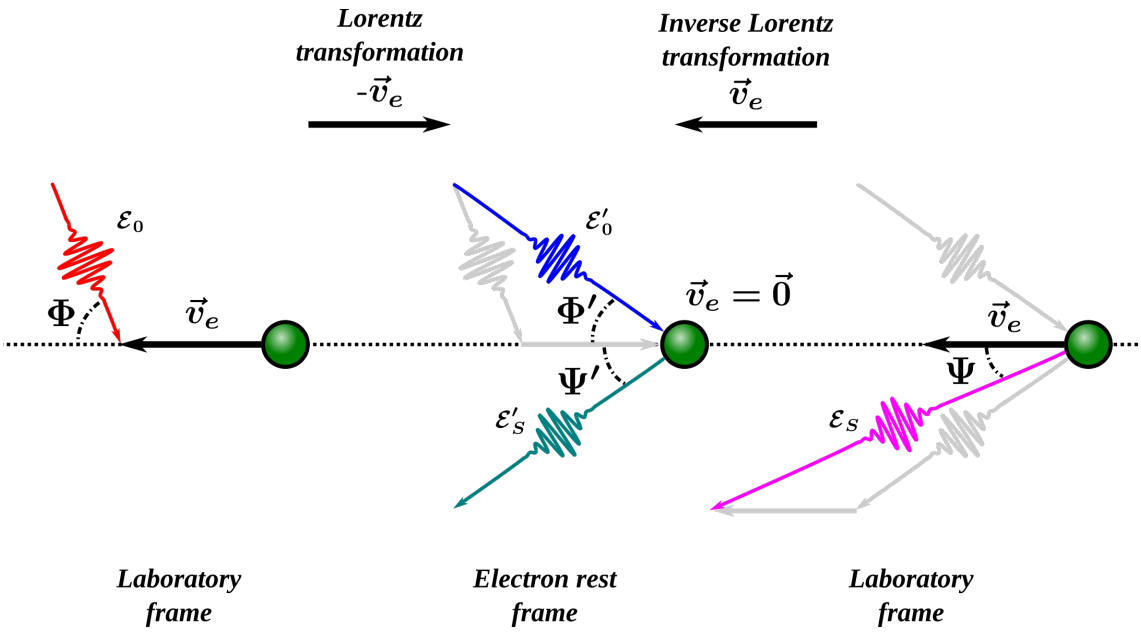

Figure 2.2: Inverse Compton scattering scheme. In the laboratory frame, photon with the energy $\mathcal{E}_0$ hits the electron with velocity $\vec{v}_e$ at the angle Φ. In the electron rest frame, incident photon with a Doppler upshifted energy $\mathcal{E}'_0$ is scattered by the electron at rest at the angle Ψ'. After moving back to the laboratory frame, the scattered angle is reduced and the scattered photon energy $\mathcal{E}_S$ increases due to the another Doppler shift.

In this section, photon scattering by the moving electron is considered. This is called *inverse Compton scattering* and it is schematically shown in vector diagrams in Fig. 2.2. In this process, the energy of the scattered photon in the laboratory frame $\mathcal{E}_S$ cannot be calculated from ordinary Compton shift equation (2.4) because for both the Compton and Thomson scattering an electron must be initially at rest. However, the equation (2.4) holds when the electron rest frame of reference is used. In the whole chapter, the upper index $\prime$ denotes physical quantities in the frame of reference, when the electron is initially at rest (ER frame) and no upper index indicates the laboratory frame (L frame).

In the L frame, the laser photon with the energy $\mathcal{E}_0$ is scattered by the electron moving with the velocity $\vec{v}_e$ at the angle of Φ according to the Fig. 2.2. One can move to the ER frame using the Lorentz transformation with the relative velocity $-\vec{v}_e$. In the new frame of reference, the electron is at rest and the photon propagates towards the electron at different angle Φ' with respect to the vector $-\vec{v}_e$. The angle Φ' satisfies the equation [8]

$$\cos\Phi' = \frac{\gamma(\cos\Phi + \beta)}{\sqrt{\sin^2\Phi + \gamma^2(\cos\Phi + \beta)^2}}, \tag{2.6}$$

where $\beta = v_e/c$ and γ is the Lorentz factor.

Moreover, after the Lorentz transformation the incident photon energy increases due to Doppler effect (also called blueshift) [7]. If the incident photon energy in the L

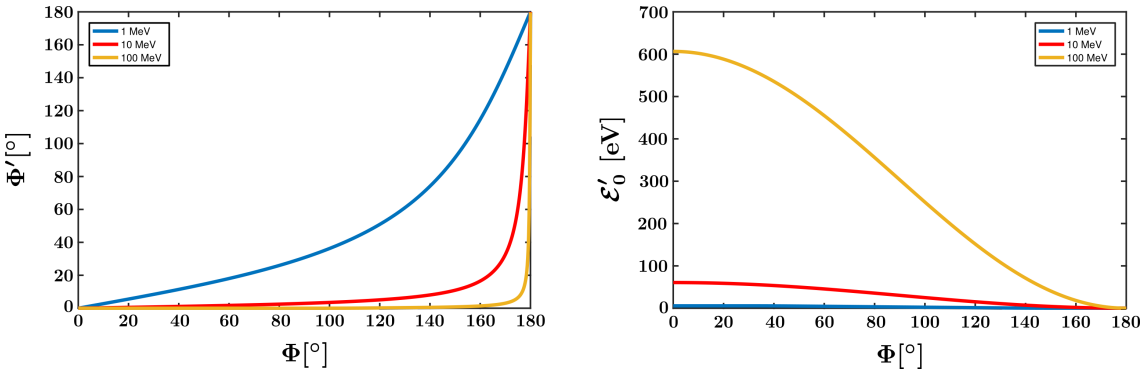

Figure 2.3: The dependence of the incidence angle Φ' and photon energy $\mathcal{E}'_0$ in ER frame versus the incidence angle Φ in L frame for 3 electrons with energies 1 MeV, 10 MeV and 100 MeV. Incident Ti:Sapphire laser photon with the energy $\mathcal{E}_0 = 1.55\,\text{eV}$ in L frame is considered.

frame is $\mathcal{E}_0$, the incident photon energy in the ER frame becomes

$$\mathcal{E}'_0 = \gamma\mathcal{E}_0(1 + \beta\cos\Phi). \tag{2.7}$$

According to the Fig. 2.3, relatively low energy electron (e.g. 1 MeV) has no significant influence on quantities in ER frame under the Lorentz transformation. On the other hand, for high energy electron (e.g. 100 MeV) there is a huge reduction of incident angle and an increase of incident photon energy. In this case the incident angle $\Phi \in (0°,147°)$ is transformed to the angle $\Phi' < 1°$ and incident photon energy $\mathcal{E}'_0$ in the ER frame is up to 400 times higher than the energy $\mathcal{E}_0$ in the L frame.

In the ER frame one can calculate Compton shift according to the equation

$$\mathcal{E}'_S = \frac{\mathcal{E}'_0}{1 + \frac{\mathcal{E}'_0}{m_e c^2}(1 + \cos(\Phi' + \Psi'))}, \tag{2.8}$$

where $\Phi' + \Psi'$ is the sum of incident and scattered angle in the ER frame (see Fig. 2.2). In this case, maximum scattered energy is for $\Phi' + \Psi' = 0\,°$. Note that equation (2.8) and (2.4) formally differ in the sign before cosine, since the definition of the angles are slightly different $(\Phi' + \Psi' = 180° - \varphi)$. One can move back to the L frame using inverse Lorentz transformation with the relative velocity $\vec{v}_e$. Scattering angle Ψ' in the ER frame is related to the scattering angle Ψ in the L frame by

$$\cos\Psi' = \frac{\gamma(\cos\Psi - \beta)}{\sqrt{\sin^2\Psi + \gamma^2(\cos\Psi - \beta)^2}} \tag{2.9}$$

and a Doppler shift for the energy of scattered photon reads

$$\mathcal{E}_S = \gamma\mathcal{E}'_S(1 + \beta\cos\Psi'). \tag{2.10}$$

Equation (2.10) is formally the same as (2.7), thus second photon energy boost occurs [8]. Additionally, equivalent angular dependency as it is shown in Fig. 2.3 is applied under the second Lorentz transformation. Therefore, due to the two successive Lorentz transformations, the angle Φ between the initial photon and electron direction collapses and has almost no effect on the final scattered photon energy.

The combination of equation (2.7),(2.8) and (2.10) gives the equation for the energy of scattered photon in L frame

$$\mathcal{E}_S = \gamma^2 \frac{\mathcal{E}_0(1+\beta\cos\Phi)}{1+\frac{\gamma\mathcal{E}_0(1+\beta\cos\Phi)}{m_e c^2}(1+\cos(\Phi'+\Psi'))}(1+\beta\cos\Psi'), \tag{2.11}$$

where the relations between Φ', Ψ', and the corresponding laboratory angles are given in equations (2.6) and (2.9). Considering the electron energies above 50 MeV ($\beta \Rightarrow 1$), head-on collision ($\Phi = 0°$) and a small scattering angle ($\Psi < 5°$), equation (2.11) can be simplified to [69]

$$\mathcal{E}_S = \frac{4\gamma^2\mathcal{E}_0}{1+\frac{4\gamma\mathcal{E}_0}{m_e c^2}+\gamma^2\Psi^2}. \tag{2.12}$$

From equation (2.11) one can calculate angular distribution of the energy of scattered photons. Maximum energy of scattered photons is reached for head-on collision with the incident angle $\Phi = 0°$. Corresponding graphs for different initial electron energies are plotted in Fig. 2.4.

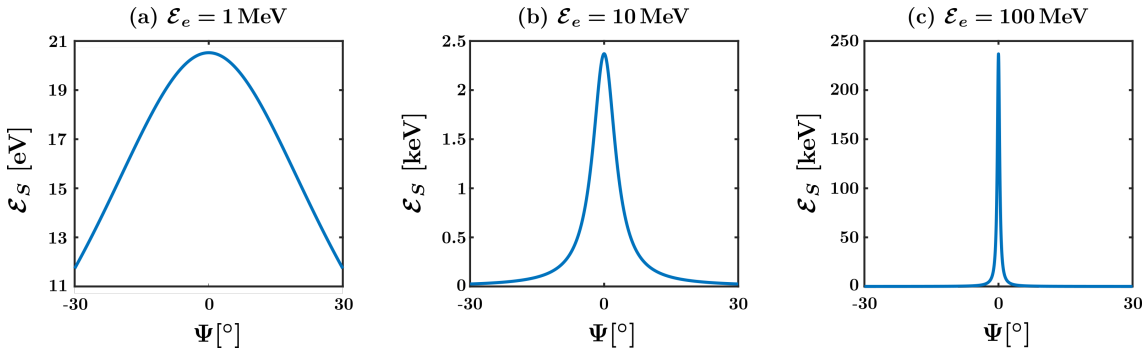

Figure 2.4: Angular distribution of the maximum energy of scattered photons for head-on collision ($\Phi = 0°$) and 3 electrons with energies 1 MeV, 10 MeV and 100 MeV and incident photon energy $\mathcal{E}_0 = 1.55$ eV in the L frame.

The divergence of the scattered photons strongly depends on the initial electron energy. When the electrons are at ultra-relativistic velocities, electron energies of the order of 10 MeV, the resulting radiation is highly collimated along the electron propagation direction. Furthermore, due to two Doppler shifts, the energy of scattered photon increases with the square of the Lorentz factor γ. The maximum energy of scattered photons is approximately

$$\mathcal{E}_S^{\max} \simeq 4\gamma^2\mathcal{E}_0. \tag{2.13}$$

For example, when the Ti:Sapphire laser photon with the energy $\mathcal{E}_0 \simeq 1.55$ eV is scattered by the counter-propagating electron with the energy 102.2 MeV ($\gamma = 200$), the maximum energy of the scattered photon reaches 248 keV and the photon travels at $\Psi = 0°$ relative to the electron direction. Thus, inverse Compton scattering using electrons from LWFA seems to be the promising way for a new generation of all-optical gamma-ray sources [70].

2.3 ICS terminology in a scientific literature

In the field of the physics of laser plasma (especially in the scientific literature), the terms such as inverse Compton scattering, Thomson backscattering, non-linear Compton scattering or only Compton or Thomson scattering are frequently used interchangeably. This relatively high freedom in using different terms is due to arbitrary choice of frame of reference.

Compton and Thomson scattering occurs in electron rest frame and differs from each other by the energy of incoming photon. The mechanism is called *Thomson scattering*, if the energy of the incident photon $\mathcal{E}_0$ is much smaller than the electron rest energy ($\mathcal{E}_0 \ll m_e c^2$), while for the incident photon energy comparable to the rest energy of electron, the term *Compton scattering* is used. However, exact border between these two mechanism does not exist. After the photon-electron interaction, due to the Compton shift, photon loses part of its energy and electron gets momentum. In the case of Thomson scattering the Compton shift of the scattered photon is negligible. For both Thomson and Compton scattering electron must be initially at rest, which can be always achieved by Lorentz transformation to the electron rest frame.

In laboratory frame, the photon scattering by the electron moving with initial velocity v_e is called the inverse Compton scattering. The term *inverse* suggests that the energy of photon increases after the scattering, in comparison to the ordinary Compton scattering. The photon energy boost is caused by the Doppler shift when the Lorentz transformation to the electron rest frame is applied. By the inverse Compton scattering it is generally meant the scattering of the photon by the counter-propagating electron, since the maximum scattered photon energy is reached. If the laser and electron are co-propagating, the term *nonlinear Thomson/Compton scattering* is sometimes used, however, the adjective *nonlinear* also suggests using laser with a strength parameter $a_0 > 1$.

Since nowadays it is still impossible to reach pure Compton scattering, even after the Lorentz transformation to the rest frame of the relativistic electron, the term *Thomson backscattering* is often used. All of these terms usually describes the same physical mechanism of the inverse Compton scattering described in section 2.2. The sources of the X- or γ-radiation based on this principle are called *Compton sources*.

Chapter 3

ICS radiation spectra

Inverse Compton scattering is a source of incoherent synchrotron radiation. This means, that in nonlinear regime ($a_0 \gg 1$), the ICS radiation spectra have similar shape as spectra of conventional synchrotron sources. In this chapter, general expression for radiation from moving charges is derived (section 3.1). According to the presented analysis, generation of X- or γ-radatiation can be achieved by the transverse oscillations of relativistic electrons. This is the key principle for the synchrotron radiation sources, which are summarized in section 3.2. Two different operating regimes can be distinguished for each synchrotron radiation source. This regimes, which are described in section 3.3 are called the undulator and the wiggler. The radiation produced in these two regimes have different qualitative and quantitative properties, which is discussed for the case of ICS in section 3.4 and 3.5.

3.1 Radiation from moving charges

Charged particle (such as an electron) moving along a curved trajectory emits a radiation. In this section, spectral intensity of the radiation from moving charge is derived. For more details, the reader is referred to Ref. [71, 72]. Without loss of generality, electron with a velocity $\boldsymbol{v}(t^\star)$, moving along the curved trajectory as it is shown in Fig. 3.1, is assumed. $\boldsymbol{r}(t^\star)$ is the position of the electron with respect to the origin of the reference frame "O". The time $t^\star$, when electron radiates, is called *retarded time*. The observer "P" at the position $\boldsymbol{x}$ receives the radiation at the *time of the observer* $t = t^\star + \Delta t$, where $\Delta t = |\boldsymbol{R}(t^\star)|/c$ is a travel time of the radiation before arriving at point "P". $\boldsymbol{R}(t^\star) = \boldsymbol{x} - \boldsymbol{r}$ is the vector from electron to the direction of observer. Corresponding unit vector to the direction of the observer is $\boldsymbol{n}(t^\star) = \boldsymbol{R}(t^\star)/|\boldsymbol{R}(t^\star)|$.

An electromagnetic field produced by the electron moving along an arbitrary curved trajectory can be derived from Maxwell equations in the form of Liénard-Wiechert

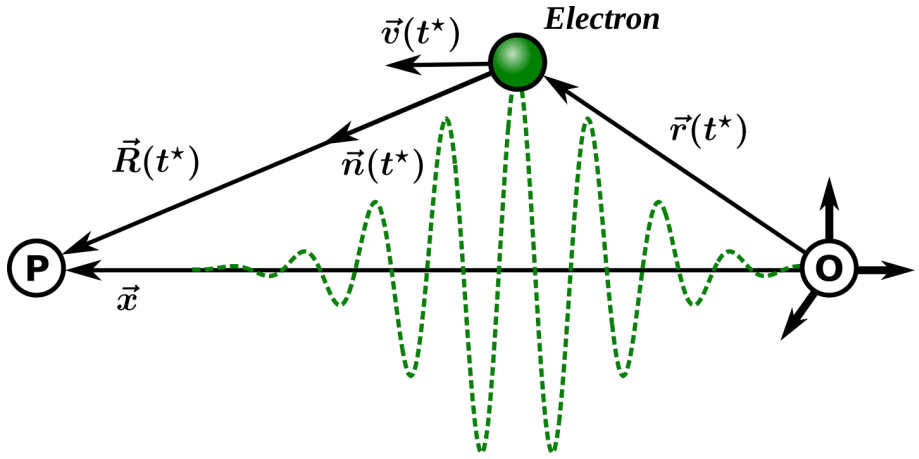

Figure 3.1: Electron moving along a curved trajectory. "O" is the origin of the reference frame, "P" the observer at the position $\boldsymbol{x}$, $\boldsymbol{r}(t^\star)$ the position of the electron, $\boldsymbol{v}(t^\star)$ electron velocity, $\boldsymbol{n}(t^\star)$ unit vector in the direction to the observer and $\boldsymbol{R}(t^\star) = \boldsymbol{x} - \boldsymbol{r}$. All quantities are at the time of radiation (retarded time) $t^\star = t - \left|\boldsymbol{R}(t^\star)\right|/c$, where t is the time when radiation reaches observer.

potentials:

$$\begin{aligned} \Phi(\boldsymbol{x},t) &= \frac{e}{4\pi\varepsilon_0}\left(\frac{1}{\kappa R(t^\star)}\right)_{ret}, \\ \boldsymbol{A}(\boldsymbol{x},t) &= \frac{e}{4\pi\varepsilon_0}\left(\frac{\boldsymbol{\beta}}{\kappa R(t^\star)}\right)_{ret}, \end{aligned} \tag{3.1}$$

where e is the electron charge, ε_0 is the vacuum permittivity, $R(t^\star) = |\boldsymbol{R}(t^\star)|$, the $\kappa = (1 - \boldsymbol{n}\cdot\boldsymbol{\beta})$ is the *contraction factor* and $\boldsymbol{\beta} = \boldsymbol{v}/c$ is the normalized electron velocity. Index "ret" suggests that the expression is evaluated in retarded time. For non-relativistic regime ($\beta \ll 1$) the contraction factor $\kappa \simeq 1$ and the equations (3.1) becomes standard electromagnetic potentials.

Using the basic relations

$$\begin{aligned} \boldsymbol{E} &= -\nabla\Phi - \frac{\partial \boldsymbol{A}}{\partial t}, \\ \boldsymbol{B} &= \nabla \times \boldsymbol{A}, \end{aligned} \tag{3.2}$$

the electromagnetic (scattered) field of the moving electron can be expressed as

$$\begin{aligned} \boldsymbol{E_S}(\boldsymbol{x},t) &= \frac{e}{4\pi\varepsilon_0}\left[\frac{(\boldsymbol{n}-\boldsymbol{\beta})(1-\boldsymbol{\beta}^2)}{\kappa^3 R^2} + \frac{\boldsymbol{n}\times[(\boldsymbol{n}-\boldsymbol{\beta})\times\dot{\boldsymbol{\beta}}]}{c\kappa^3 R}\right]_{ret}, \\ \boldsymbol{B_S}(\boldsymbol{x},t) &= \frac{1}{c}\left[\boldsymbol{n}\times\boldsymbol{E_S}\right]_{ret}. \end{aligned} \tag{3.3}$$

The first term on the RHS of the equation (3.3) for the E-field is called *velocity field*. It falls off as $1/R^2$ and is just the generalisation of Coulomb's law to uniformly moving charges. The second term is the *radiation field* $\boldsymbol{E_R}$. It falls off as $1/R$, is proportional to the electron acceleration $\dot{\boldsymbol{\beta}}$ and is perpendicular to $\boldsymbol{n}$.

The radiation power emitted per solid angle reads [72]

$$\frac{dP(t)}{d\Omega} = |\boldsymbol{A}(t)|^2, \tag{3.4}$$

where

$$\boldsymbol{A}(t) = \sqrt{c\varepsilon_0} \cdot [R\boldsymbol{E}_{\boldsymbol{R}}]_{ret}. \tag{3.5}$$

The integration of the equation (3.4) over time of the observer gives the total energy radiated by an electron per solid angle

$$\frac{dW}{d\Omega} = \int_{-\infty}^{\infty} |\boldsymbol{A}(t)|^2 dt. \tag{3.6}$$

Taking the Fourier transform

$$\boldsymbol{A}(\omega) = \frac{1}{\sqrt{2\pi}} \int_{-\infty}^{\infty} \boldsymbol{A}(t) e^{i\omega t} dt, \tag{3.7}$$

$$\boldsymbol{A}(t) = \frac{1}{\sqrt{2\pi}} \int_{-\infty}^{\infty} \boldsymbol{A}(\omega) e^{-i\omega t} d\omega, \tag{3.8}$$

and using Parseval's theorem [73], equation (3.6) can be written in the form

$$\frac{dW}{d\Omega} = \int_{-\infty}^{\infty} |\boldsymbol{A}(\omega)|^2 d\omega. \tag{3.9}$$

Since negative frequencies has no physical meaning, the following equation

$$\frac{dW}{d\Omega} = \int_{0}^{\infty} \frac{d^2 I}{d\omega d\Omega} d\omega \tag{3.10}$$

can be used to define a quantity

$$\frac{d^2 I}{d\omega d\Omega} = |\boldsymbol{A}(\omega)|^2 + |\boldsymbol{A}(-\omega)|^2, \tag{3.11}$$

which can be identified as the radiation energy per unit solid angle per unit frequency. This quantity is usually called *spectral intensity of radiation*. If $\boldsymbol{A}(t)$ is real, then according to (3.7) $\boldsymbol{A}(-\omega) = \overline{\boldsymbol{A}}(\omega)$ and spectral intensity of radiation yields

$$\frac{d^2 I}{d\omega d\Omega} = 2|\boldsymbol{A}(\omega)|^2. \tag{3.12}$$

Fourier transform (3.7) of the quantity $\boldsymbol{A}(t)$ given by the equation (3.5) reads

$$\boldsymbol{A}(\omega) = \left(\frac{e^2}{32\pi^3 \varepsilon_0 c}\right)^{1/2} \int_{-\infty}^{\infty} e^{i\omega t} \left[\frac{\boldsymbol{n} \times [(\boldsymbol{n} - \boldsymbol{\beta}) \times \dot{\boldsymbol{\beta}}]}{\kappa^3}\right]_{ret} dt. \tag{3.13}$$

By changing integration variable t to retarded time $t^\star$, one can write

$$\boldsymbol{A}(\omega) = \left(\frac{e^2}{32\pi^3 \varepsilon_0 c}\right)^{1/2} \int_{-\infty}^{\infty} e^{i\omega\left(t^\star + \frac{R(t^\star)}{c}\right)} \frac{\boldsymbol{n} \times [(\boldsymbol{n} - \boldsymbol{\beta}) \times \dot{\boldsymbol{\beta}}]}{\kappa^2} dt^\star. \tag{3.14}$$

Moreover, the observer is considered to be at the far distance away from the electron, thus $R(t^\star)$ can be approximated by the

$$R(t^\star) \simeq x - \boldsymbol{n} \cdot \boldsymbol{r}(t^\star). \tag{3.15}$$

Eventually, after the combination of equations (3.12), (3.14), (3.15) and with using $\kappa = (1 - \boldsymbol{n} \cdot \boldsymbol{\beta})$ and omitting the phase shift, the usual form of the spectral intensity of radiation can be derived:

$$\frac{d^2 I}{d\omega d\Omega} = \frac{e^2}{16\pi^3 \varepsilon_0 c} \left| \int_{-\infty}^{\infty} e^{i\omega \left(t^\star - \frac{\boldsymbol{n} \cdot \boldsymbol{r}(t^\star)}{c} \right)} \frac{\boldsymbol{n} \times [(\boldsymbol{n} - \boldsymbol{\beta}) \times \dot{\boldsymbol{\beta}}]}{(1 - \boldsymbol{n} \cdot \boldsymbol{\beta})^2} dt^\star \right|^2 . \tag{3.16}$$

One can obtain some characteristic features of the radiation directly from the equation (3.16) [74]:

1. Relativistic electron ($|\boldsymbol{\beta}| \simeq 1$) moving in direction to observer ($\boldsymbol{\beta} \parallel \boldsymbol{n}$) radiates much more than non-relativistic, because for such relativistic electron the contraction factor $(1 - \boldsymbol{n} \cdot \boldsymbol{\beta})$, which is in denominator, goes to zero.
2. There is no radiation if the electron acceleration $\dot{\boldsymbol{\beta}} = \vec{0}$, since the integral in the equation (3.16) equals zero. With increasing $\dot{\boldsymbol{\beta}}$, electron radiates more.
3. In order to obtain high radiated energy, it is much more efficient to use transverse force than the longitudinal, because according to the special theory of relativity the force in Newton's second law is given by

   $$\boldsymbol{F} = \gamma^3 m_e \boldsymbol{a}_\parallel + \gamma m_e \boldsymbol{a}_\perp \tag{3.17}$$

   therefore $\dot{\boldsymbol{\beta}}_\parallel \propto \boldsymbol{F}_\parallel / \gamma^3$ a $\dot{\boldsymbol{\beta}}_\perp \propto \boldsymbol{F}_\perp / \gamma$ [75].
4. Electron radiates at the higher frequency $\omega \simeq 2\gamma^2 \omega_e$, where ω_e is the frequency of electron velocity variation. It is based on the fact that the integration over time gives a nonzero result only when the integrand, excluding the exponential, varies approximately at the same frequency as the phase term, $\omega(1 - \beta) \simeq \omega_e$.

3.2 Synchrotron light sources

The previous analysis predicts generation of X- or γ-radiation by the transverse oscillations of relativistic electrons. This is the key principle for the synchrotron radiation sources. Electrons are first accelerated either in conventional accelerator or in plasma and then due to the external force they start to oscillate in the direction perpendicular to the direction of propagation. According to the type of accelerator and the type of oscillating device (undulator), several different schemes for generation of synchrotron radiation were proposed:

- *Betatron radiation sources* uses plasma for both accelerating electrons and bending their trajectories. In the section 1.5, LWFA mechanism for accelerating electrons in the bubble regime was described. Electrons trapped into the ion cavity in the wake behind the laser are not only accelerated, but also due to the transverse electrostatic field oscillate perpendicularly to the direction of propagation with the (betatron) frequency $\omega_b = \omega_p/\sqrt{2\gamma}$, where ω_p is the plasma frequency given by (1.2). Due to these oscillations electrons produce the so-called betatron radiation.
- *Conventional synchrotrons:* electrons are accelerated either in plasma or in conventional accelerator and then directed into the conventional undulator, where the electron trajectory is wiggled. Conventional undulator consists of a periodic structure of dipole magnets. Electron propagating along this periodic magnet structure is forced to undergo oscillations and thus radiate energy.
- *Inverse Compton scattering:* electrons accelerated in plasma or in conventional accelerator are aimed against counter-propagating laser pulse, whose electromagnetic field serves as an undulator and forces electrons to oscillate. As a result, electrons are again the source of synchrotron-like radiation.

Table 3.1 gives typical parameters and features as well as scaling laws for the sychrotron sources reviewed in this section. In comparison to the other synchrotron radiation sources, the source based on the inverse Compton scattering produce radiation with the highest photon energy and relatively low divergence ($\sim mrad$). However the photon yield is the lowest among the other sources.

Parametry	γ	λ_u	N	N_e	$\hbar\omega_c$	θ_r $(mrad)$	N_γ
Betatron	200	150 μm	3	10^9	5 keV	50.0	$\sim 10^9$
Synchrotron	400	1 cm	100	10^8	25 eV	2.5	$\sim 10^8$
ICS	400	0.4 μm	10	10^8	650 keV	2.5	$\sim 10^7$

Table 3.1: The typical features for the different synchrotron radiation sources achievable with a 50 TW-class laser. The values represent the orders of magnitude of the parameters: the Lorentz factor γ, the electron oscillation wavelength λ_u, the number of electron oscillations N, the number of electrons N_e, the critical frequency ω_c, the radiation divergence θ_r and the number of photons N_γ. Data from [74].

3.3 Undulator and wiggler regime

Electron moving to the negative direction of the x axis and oscillating in the direction of y axis is considered. In the L frame, due to the Lorentz transformation, electron radiates within the opening angle $\vartheta \sim 1/\gamma$ of the radiation cone [74]. For ultra-relativistic electrons ($\gamma \sim 100$), the angle ϑ is of the order of mrad. Two different regimes can be distinguished for each synchrotron radiation source, discussed in the section 3.2. Undulator regime is depicted in Fig. 3.2a. In this regime, electron radiates all along the trajectory in the same direction. This happens when the maximum angle Ω between the electron velocity and the propagation direction is smaller then the opening angle of radiation cone ϑ. One can define *the characteristic parameter* $K = \Omega/\vartheta$, then for undulator regime holds $K \ll 1$. The situation is exactly the opposite for the wiggler regime (Fig. 3.2b), where the electron radiates in the different section of the trajectory in different directions. This occurs when $\Omega \gg \vartheta$, hence the characteristic parameter $K \gg 1$.

The radiation produced in these two regimes have different qualitative and quantitative properties in terms of spectrum, divergence, radiated energy and number of emitted photons [74]. in the case of the radiation by ICS, the characteristic parameter $K = a_0$, where a_0 is the laser strength parameter described by the equation (1.1). Table 1.1 shows, that the threshold between undulator and wiggler regime for ICS corresponds to the laser intensity $2.16 \cdot 10^{18}$ W/cm^2 (for $\lambda_L = 0.8\,\mu$m). Lasers with such intensity (and even higher) are currently available, therefore both regimes should receive considerable attention in ICS experiments as well as in theoretical studies.

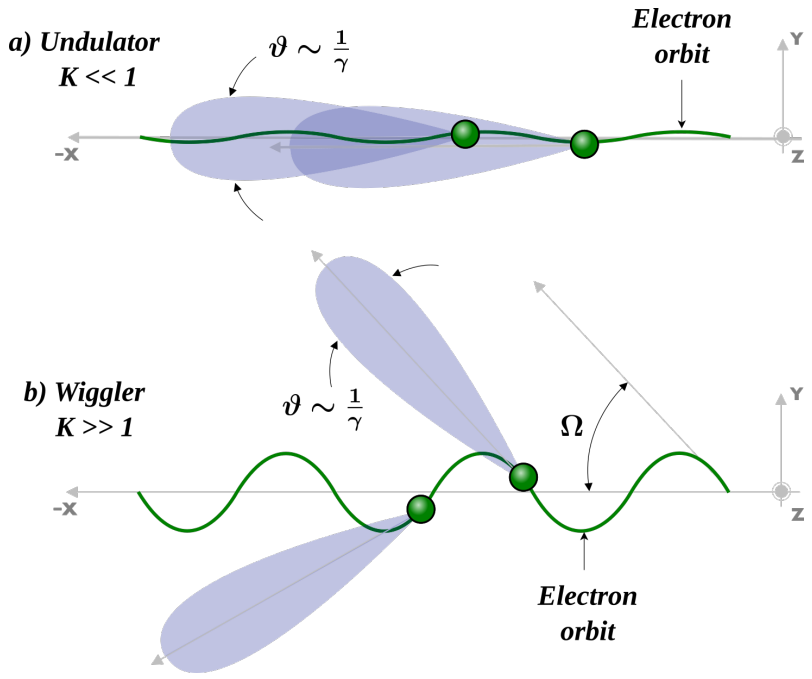

Figure 3.2: Illustration of the undulator and wiggler regime. Electron is moving along the x axis, oscillating in the direction of y axis and radiates within the opening angle ϑ. Ω is the maximal angle of the electron trajectory and $K = \Omega/\vartheta$ is the characteristic parameter.

3.4 Spectrum shape

The electron trajectory can be approximated as a transverse sinusoidal oscillation. In the case of $a_0 \ll 1$ (undulator regime), the motion contains only the fundamental component and the spectrum consists of a single peak at the fundamental frequency ω_1, which corresponds to the energy of the scattered photon given by (2.11). The energy depends on the angle of observation and reaches its maximum in the case of head-on collision.

For $a_0 \gg 1$ the trajectory in the average rest frame is a well-known figure-eight motion and contains many harmonics of the fundamental. In the laboratory frame, $\boldsymbol{v} \times \boldsymbol{B}$ force gives rise to the broadening of the spectral components. Analytic expression for synchrotron-like spectra can be obtained.

The equation (3.16) can be rewritten as follows

$$\frac{\mathrm{d}^2 I}{\mathrm{d}\omega\,\mathrm{d}\Omega} = \int_{-\infty}^{\infty} \frac{\mathrm{d}P(\boldsymbol{n},\omega,t)}{\mathrm{d}\omega \mathrm{d}\Omega}\,\mathrm{d}t, \tag{3.18}$$

where $P(\boldsymbol{n},\omega,t)/(\mathrm{d}\omega\mathrm{d}\Omega)$ is radiation power emitted per unit solid angle per unit frequency in the direction to the observer $\boldsymbol{n}$. The integration of (3.18) over solid angle gives

$$\frac{\mathrm{d}I}{\mathrm{d}\omega} = \int_{-\infty}^{\infty} \frac{\mathrm{d}P(\omega,t)}{\mathrm{d}\omega}\,\mathrm{d}t, \tag{3.19}$$

where $P(\omega,t)/\mathrm{d}\omega$ is radiation power emitted in time t per unit frequency. This can be analytically calculated assuming synchrotron radiation [76] according to

$$\frac{\mathrm{d}P(\omega,t)}{\mathrm{d}\omega} = \frac{1}{4\pi\varepsilon_0}\frac{\sqrt{3}q^2\gamma}{2\pi\rho}\frac{\omega}{\omega_c}\int_{\frac{\omega}{\omega_c}}^{\infty} K_{5/3}(\eta)\mathrm{d}\eta, \tag{3.20}$$

where $\omega_c = 3\gamma^3 c/(2\rho)$ is a critical frequency, $K_{5/3}(\eta)$ is the modified Bessel function of the second kind [77]. Radius of curvature ρ can be obtained from

$$\rho = \left| \frac{(v_\parallel^2 + v_\perp^2)^{3/2}}{v_\parallel a_\perp - v_\perp a_\parallel} \right|, \tag{3.21}$$

where $v_\parallel$ (resp. $a_\parallel$) is a velocity (resp. acceleration) of the electron in the direction of propagation and $v_\perp$ (resp. $a_\perp$) is transverse velocity (resp. transverse acceleration). This model can be used only for $a_0 \gg 1$.

3.5 Radiation properties

In the case of undulator ($a_0 \ll 1$), the mean energy of photons after integrating over the angular distribution yields $\mathcal{E}_m^{\text{total}} \simeq \mathcal{E}_m^{\text{on-axis}}/2$. The number of emitted photons per period and per electron at the energy $\mathcal{E}_m^{\text{total}}$ in practical units reads [74]

$$N_\gamma \simeq 1.53 \cdot 10^{-2} \cdot a_0^2 \qquad a_0 \ll 1. \tag{3.22}$$

When wiggler regime is considered ($a_0 \gg 1$), the spectrum is synchrotron-like with the critical energy estimated as

$$\mathcal{E}_c = \frac{6\pi a_0 \gamma^2 \hbar c}{\lambda_L}, \tag{3.23}$$

where λ_L is the laser wavelength. The mean energy for synchrotron spectrum is approximately $\mathcal{E}_m^{\text{total}} \simeq 0.3\mathcal{E}_c$. The number of emitted photons per period and per electron at the mean energy in practical units reads

$$N_\gamma \simeq 3.31 \cdot 10^{-2} \cdot a_0 \qquad a_0 \gg 1. \tag{3.24}$$

In laser-plasma accelerators, electrons are randomly distributed inside the bunch at the X-ray wavelength scale, and the radiation is incoherently summed. The total spectral intensity is therefore equal to

$$\left.\frac{\mathrm{d}^2 I}{\mathrm{d}\omega\,\mathrm{d}\Omega}\right|_{N_e} = N_e \left.\frac{\mathrm{d}^2 I}{\mathrm{d}\omega\,\mathrm{d}\Omega}\right|_{N_e=1}, \tag{3.25}$$

where N_e is the number of electrons. Electrons in the bunch interacts with its own radiation. Under certain conditions this can lead to a microbunching of the electron distribution within a bunch at the fundamental wavelength of the radiation and its harmonics, then the radiation would be coherently summed as follows

$$\left.\frac{\mathrm{d}^2 I}{\mathrm{d}\omega\,\mathrm{d}\Omega}\right|_{N_e} = N_e^2 \left.\frac{\mathrm{d}^2 I}{\mathrm{d}\omega\,\mathrm{d}\Omega}\right|_{N_e=1}. \tag{3.26}$$

This mechanism is called free-electron laser (FEL). The radiation is orders of magnitude higher than in conventional synchrotron-like sources. However, it is even challenge in conventional synchrotron facilities to fulfill conditions for FEL. In the case of ICS the electron distribution remains random along the propagation and the radiation is incoherent [74].

Chapter 4

$\mathcal{COCO}$ simulations of the ICS

There are several codes which can be used for simulations of ICS, e.g. EPOCH [22] and OSIRIS [78]. In such codes radiation is usually calculated using Monte Carlo method or by ordinary numerical integration of the equation (3.16). This can be very demanding on computing time. Moreover, the stochastic approach, which is used for example in EPOCH, is possible only for high values of laser strength parameter a_0, when radiation is synchrotron-like. These codes usually cover a large amount of physical phenomena, thus it could be relatively complicated for experimentalists, interested only in radiation properties of ICS.

Therefore, new and relatively fast, low limit ICS "**Co**mpton **co**de" ($\mathcal{COCO}$) is presented in this chapter. This code is implemented in Matlab, which is widely used among experimentalists and offers easy way to display and save graphs. In $\mathcal{COCO}$ simulation, electron equations of motion are solved and radiation spectra are calculated using fast Fourier transform. The typical scheme of $\mathcal{COCO}$ simulation is depicted in Fig. 4.1 and it is described in detail further in this chapter.

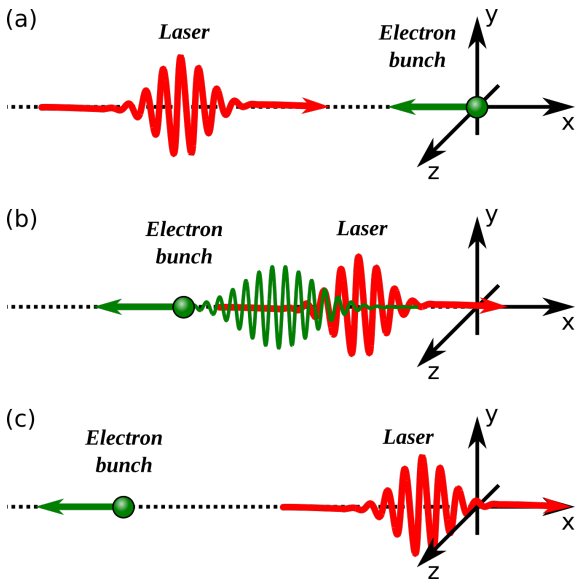

Figure 4.1: Scheme of the typical $\mathcal{COCO}$ simulation of ICS: (a) the start of the simulation, (b) simulation in progress, (c) the end of the simulation.

4.1 Simulation setup

$\mathcal{COCO}$ simulation is controlled trough the input file (`inputdeck.m`), which is described in detail in Appendix B. This file is located in the main folder of the simulation package (see Appendix A). Here, the electron bunch configuration, parameters of a laser, position of the observer and other setting necessary for running the code are defined. User can easily change the default settings in `inputdeck.m` and run own simulation. In this section, laser and electron bunch initialization is presented.

4.1.1 Laser setup

Before the laser initialization, the parameters of the laser must be set in `inputdeck.m`. Most important parameters are: the laser strength parameter a_0 (`a0`), the laser wavelength λ_0 (`l0`), full width at half maximum FWHM for Gaussian temporal profile (`FWHM`) and beam waist σ_0 for Gaussian beam (`sig0`).

Afterwards, in the file `calculateDerivedQuantities.m` the other laser parameters are derived: the laser intensity I from the equation (1.1), the electric field amplitude $U_0 = \sqrt{\frac{2I}{\varepsilon_0 c}}$, the laser wave number $k = 2\pi/\lambda_0$, the laser frequency $\omega_0 = ck$, the energy of the laser photon $\mathcal{E}_0 = \omega_0\hbar$, the laser period $T = 2\pi/\omega_0$, the Rayleigh length for Gaussian beam $x_0 = \frac{\pi\sigma_0^2}{\lambda_0}$ and the quantity $t_0 = \mathrm{FWHM}/(2\sqrt{2\log 2})$.

In the basic $\mathcal{COCO}$ simulation, five different models of the laser are implemented:

1. Electromagnetic plane wave (`cos_none`):

$$\begin{aligned} \mathcal{P}(x,t) &= U_0 \cos(kx - \omega_0 t), \\ \boldsymbol{E} &= \mathcal{P}(x,t)\hat{\boldsymbol{y}}, \\ \boldsymbol{B} &= \frac{\mathcal{P}(x,t)}{c}\hat{\boldsymbol{z}}. \end{aligned} \tag{4.1}$$

2. Electromagnetic plane wave with rectangular temporal profile (`cos_rec`):

$$\begin{aligned} \boldsymbol{E} &= \mathcal{P}(x,t)\mathcal{H}\left(t + \frac{\mathrm{FWHM}}{2}\right)\mathcal{H}\left(-t + \frac{\mathrm{FWHM}}{2}\right)\hat{\boldsymbol{y}}, \\ \boldsymbol{B} &= \frac{\mathcal{P}(x,t)}{c}\mathcal{H}\left(t + \frac{\mathrm{FWHM}}{2}\right)\mathcal{H}\left(-t + \frac{\mathrm{FWHM}}{2}\right)\hat{\boldsymbol{z}}, \end{aligned} \tag{4.2}$$

   where $\mathcal{H}$ is the Heaviside step function.

3. Electromagnetic plane wave with $\cos^2$ temporal profile (`cos_cos2`):

$$\begin{aligned} \boldsymbol{E} &= \mathcal{P}(x,t)\cos^2\left(\frac{t}{t_0}\right)\hat{\boldsymbol{y}}, \\ \boldsymbol{B} &= \frac{\mathcal{P}(x,t)}{c}\cos^2\left(\frac{t}{t_0}\right)\hat{\boldsymbol{z}}, \end{aligned} \tag{4.3}$$

4. Electromagnetic plane wave with Gaussian temporal profile (`cos_gauss`):

$$\begin{aligned} \boldsymbol{E} &= \mathcal{P}(x,t) \exp\left[-2{,}77\left(\frac{t}{\mathrm{FWHM}}\right)^2\right]\hat{\boldsymbol{y}}, \\ \boldsymbol{B} &= \frac{\mathcal{P}(x,t)}{c} \exp\left[-2{,}77\left(\frac{t}{\mathrm{FWHM}}\right)^2\right]\hat{\boldsymbol{z}}, \end{aligned} \tag{4.4}$$

5. Gaussian beam with Gaussian temporal profile (`gauss_gauss`) [79]:

$$\begin{aligned} \boldsymbol{E} &= \mathcal{U}(x,r,t)\hat{\boldsymbol{y}}, \\ \boldsymbol{B} &= \frac{\mathcal{U}(x,r,t)}{c}\hat{\boldsymbol{z}}, \end{aligned} \tag{4.5}$$

where

$$\begin{aligned} \mathcal{U}(x,r,t) &= U_0\frac{\sigma_0}{\sigma(x)} \cdot U_1(x,r,t) \cdot U_2(x,r) \cdot U_3(x,r,t) \cdot U_4(x), \\ U_1(x,r,t) &= \exp\left[-\frac{\mathcal{T}^2}{2t_0^2}\right], \\ U_2(x,r) &= \exp\left[-\frac{r^2}{\sigma^2(x)} + \frac{r^4}{2\sigma^4(x)}\left(\frac{1}{t_0\omega_0}\right)^2\right], \\ U_3(x,r,t) &= \exp\left[i\omega_0\left(1 - \frac{r^2}{\sigma^2(x)}\left(\frac{1}{t_0\omega_0}\right)^2\right)\mathcal{T}\right], \\ U_4(x) &= \exp\left[i\varphi(x)\right], \end{aligned} \tag{4.6}$$

where $r = \sqrt{y^2 + z^2}$. The square beam radius $\sigma(x)$, Gouy phase $\varphi(x)$, radius of curvature $R(x)$ and the function $\mathcal{T}$ are defined as follows:

$$\begin{aligned} \sigma(x) &= \sigma_0\sqrt{1 + \left(\frac{x}{x_0}\right)^2}, \\ \varphi(x) &= \tan^{-1}\frac{x}{x_0}, \\ R(x) &= x\left[1 + \left(\frac{x_0}{x}\right)^2\right], \\ \mathcal{T} &= \left(t - \frac{r^2}{2cR(x)} - \frac{x}{c}\right). \end{aligned} \tag{4.7}$$

Switching between these models can be done by setting the variable `laser` in `inputdeck.m`. All models uses linear polarization by default, however, the polarization can be modified easily in the definition of the laser models in the file `setLaser.m`. In this file, user can add own model of laser as well.

4.1.2 Electron bunch configuration

Electron bunch is initialized through the file `setElectrons.m`. In $\mathcal{COCO}$ simulation electron bunch contains N_e (`el_num`) electrons with energies $\mathcal{E}_e$ normally distributed around a mean electron energy $\mathcal{E}_m$ (`el_en`) with standard deviation $\mathcal{E}_\sigma$ (`el_spread`).

An absolute value of the initial momentum p_e, Lorentz factor γ and normalized velocity β is calculated for each electron:

$$p_e = \frac{\sqrt{\mathcal{E}_e^2 - m_e^2 c^4}}{c}, \qquad \gamma = \frac{\mathcal{E}_e}{m_e c^2}, \qquad \beta = \frac{p_e}{m_e \gamma c}. \tag{4.8}$$

The expected mean energy of the scattered photons $\mathcal{E}_m$ is calculated according to the equation (2.11).

The center of the electron bunch is at the origin and the size of the bunch is defined by the vector $\boldsymbol{l} = (l_x, l_x, l_z)$ (`el_size`). The initial position $\boldsymbol{r}_0$ of each electron is then randomly distributed within the bunch as follows

$$\begin{aligned} r_x^{(0)} &= l_x \cdot \mathcal{R}_1, \\ r_y^{(0)} &= l_y \cdot \mathcal{R}_2, \\ r_z^{(0)} &= l_z \cdot \mathcal{R}_3, \end{aligned} \tag{4.9}$$

where $\mathcal{R}_1$, $\mathcal{R}_2$ and $\mathcal{R}_3$ are a uniformly distributed random numbers from the interval (-0.5,0.5).

By default, electron is moving in the negative direction of the x axis. One can adjust the direction of the bunch by setting the angles φ_e (`el_phi`) and θ_e (`el_the`) according to Fig. 4.2. The divergence of the electron bunch can be defined by the quantities $\Delta\varphi_e$ (`el_phi_div`) and $\Delta\theta_e$ (`el_theta_div`) which randomly modifies angles for each electron in the bunch as follows

$$\begin{aligned} \varphi_e^{\mathcal{R}} &= \varphi_e + \Delta\varphi_e \cdot \mathcal{R}_4, \\ \theta_e^{\mathcal{R}} &= \theta_e + \Delta\theta_e \cdot \mathcal{R}_5, \end{aligned} \tag{4.10}$$

where $\mathcal{R}_4$ and $\mathcal{R}_5$ are a uniformly distributed random numbers from the interval (-0.5,0.5).

Eventually, electron momentum is calculated:

$$\begin{aligned} p_x^{(0)} &= -p_e \cos(\varphi_e^{\mathcal{R}}) \cos(\theta_e^{\mathcal{R}}), \\ p_y^{(0)} &= p_e \sin(\varphi_e^{\mathcal{R}}), \\ p_z^{(0)} &= p_e \cos(\varphi_e^{\mathcal{R}}) \sin(\theta_e^{\mathcal{R}}). \end{aligned} \tag{4.11}$$

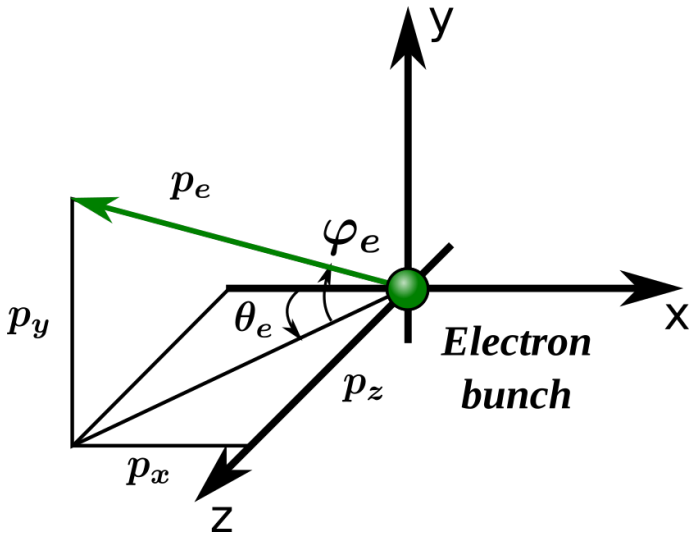

Figure 4.2: Electron bunch configuration. Initial propagation direction of the electron bunch is set by the angles φ_e and θ_e. Initial momentum p_e is calculate according to the equation (4.8).

4.2 Electron equations of motion solver

The relativistic motion of the electron with velocity $\boldsymbol{v}$ and charge e in the presence of electromagnetic field is described by set of first order differential equations of motion with Lorentz force on the right side

$$\frac{\mathrm{d}\boldsymbol{p}}{\mathrm{d}t} = e(\boldsymbol{E} + \boldsymbol{v} \times \boldsymbol{B}), \tag{4.12}$$

where $\boldsymbol{E}$ and $\boldsymbol{B}$ are electric field and magnetic field respectively and

$$\boldsymbol{p} = \gamma m_e \boldsymbol{v} \tag{4.13}$$

is the electron momentum. Combination of the equation (4.13), definition of Lorentz factor γ (1.9) and the equation for total energy of an electron $\mathcal{E} = \sqrt{m_e^2c^4 + \boldsymbol{p}^2c^2}$ gives particle velocity in the form

$$\boldsymbol{v} = \frac{\mathrm{d}\boldsymbol{r}}{\mathrm{d}t} = \frac{\boldsymbol{p}c^2}{\sqrt{m_e^2c^4 + \boldsymbol{p}^2c^2}}. \tag{4.14}$$

In the $\mathcal{COCO}$ simulation, electron trajectory is calculated in retarded time $t^\star$ by solving six differential equation (4.12) and (4.14) with regard to the initial conditions $\boldsymbol{r^{(0)}} = (r_x^{(0)}, r_y^{(0)}, r_z^{(0)})$ and $\boldsymbol{p^{(0)}} = (p_x^{(0)}, p_y^{(0)}, p_z^{(0)})$ described in the section 4.1.2. Time evolution of an electromagnetic field ($\boldsymbol{E}(t^\star)$ and $\boldsymbol{B}(t^\star)$) were defined according to the section 4.1.1.

Differential equation for the electron momentum

$$\frac{\mathrm{d}\boldsymbol{p}}{\mathrm{d}t^\star} = \boldsymbol{\mathcal{L}}(\boldsymbol{v},t^\star), \qquad \boldsymbol{p}(0) = \boldsymbol{p^{(0)}} = (p_x^{(0)}, p_y^{(0)}, p_z^{(0)}), \tag{4.15}$$

where $\boldsymbol{\mathcal{L}}(\boldsymbol{v},t^\star)$ is the Lorentz force, is solved using the 4th order Runge-Kutta scheme:

$$\begin{aligned}
\boldsymbol{k_1} &= \boldsymbol{\mathcal{L}}(t^{\star(n)}, \boldsymbol{v^{(n)}}) \\
\boldsymbol{k_2} &= \boldsymbol{\mathcal{L}}(t^{\star(n)} + \frac{\Delta t^\star}{2}, \boldsymbol{v^{(n)}} + \frac{\Delta t^\star}{2}\boldsymbol{k_1}), \\
\boldsymbol{k_3} &= \boldsymbol{\mathcal{L}}(t^{\star(n)} + \frac{\Delta t^\star}{2}, \boldsymbol{v^{(n)}} + \frac{\Delta t^\star}{2}\boldsymbol{k_2}), \\
\boldsymbol{k_4} &= \boldsymbol{\mathcal{L}}(t^{\star(n)} + \Delta t^\star, \boldsymbol{v^{(n)}} + \Delta t^\star \boldsymbol{k_3}), \\
\boldsymbol{p^{(n+1)}} &= \boldsymbol{p^{(n)}} + \frac{\Delta t^\star}{6}(\boldsymbol{k_1} + 2\boldsymbol{k_2} + 2\boldsymbol{k_3} + \boldsymbol{k_4}),
\end{aligned} \tag{4.16}$$

where $\Delta t^\star$ is a time step. Equation for electron position

$$\frac{\mathrm{d}\boldsymbol{r}}{\mathrm{d}t^\star} = \boldsymbol{\mathcal{V}}(\boldsymbol{p},t^\star), \qquad \boldsymbol{r^{(0)}} = (r_x^{(0)}, r_y^{(0)}, r_z^{(0)}), \tag{4.17}$$

where $\boldsymbol{\mathcal{V}}(\boldsymbol{p},t^\star)$ is the RHS of the equation (4.14) is then solved using the standard Euler method:

$$\boldsymbol{r^{(n+1)}} = \boldsymbol{r^{(n)}} + \Delta t^\star \boldsymbol{\mathcal{V}}(\boldsymbol{p^{(n)}},t^{\star(n)}). \tag{4.18}$$

Using Runge-Kutta scheme for calculating electron position is unnecessary, since $\boldsymbol{v^{(n)}}$ is already known at the beginning of each cycle. Equation 4.19 becomes

$$\boldsymbol{r^{(n+1)}} = \boldsymbol{r^{(n)}} + \Delta t^\star \boldsymbol{v^{(n)}}. \tag{4.19}$$

For increasing accuracy, a smaller time step $\Delta t^\star$ should be set in `inputdeck.m`.

4.3 Spectra calculation

In *COCO* simulation, radiation spectra for the observer in the far distance away from the electron are investigated. Scheme of such configuration is depicted in Fig. 4.3. According to the equation (3.12) the spectral intensity of radiation has following form

$$\frac{d^2I}{d\omega d\Omega} = 2|\boldsymbol{A}(\omega)|^2. \tag{4.20}$$

Furthermore, equation (3.7) can be rewritten using the symbol of Fourier transform:

$$\boldsymbol{A}(\omega) = \frac{1}{\sqrt{2\pi}}\mathfrak{F}[\boldsymbol{A}(t)], \tag{4.21}$$

where

$$\boldsymbol{A}(t) = \sqrt{c\varepsilon_0}\cdot[R\boldsymbol{E_R}]_{ret}\,. \tag{4.22}$$

The combination of equations (4.20), (4.21) and (4.22) gives

$$\frac{d^2I}{d\omega d\Omega} = \frac{c\varepsilon_0}{\pi}\left|\mathfrak{F}\left[R\boldsymbol{E_R}\right]_{ret}\right|^2, \tag{4.23}$$

which is another expression for spectral intensity of radiation, equivalent to (3.16). In other words, radiation spectra can be obtained as a Fourier transform of the radiation field $\boldsymbol{E_R}$ (the second term of the RHS of the equation (3.3)).

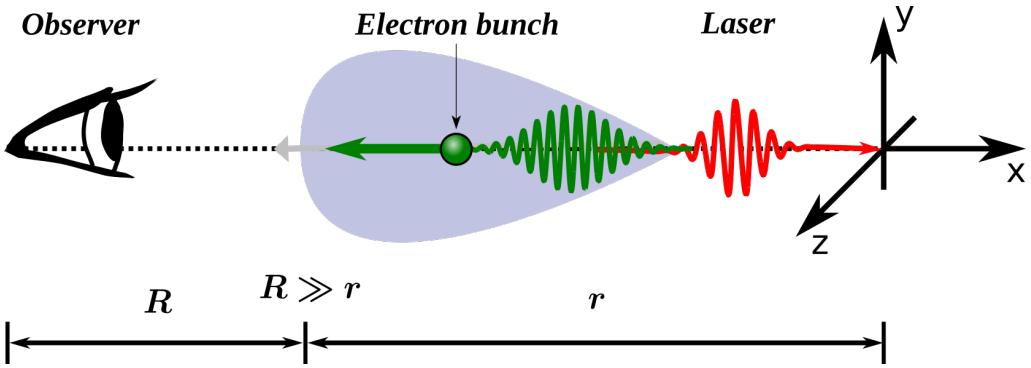

Figure 4.3: Radiation spectra is calculated for an observer in the far distance away from the electron ($R \gg r$).

4.3.1 Radiation field of the electron

In *COCO* simulation, the electron trajectory (section 4.2) was solved for the $N_{t^\star}$ points of the retarded time $t^\star$. Desired sampling can be adjusted in `inputdeck.m` by setting the time step $\Delta t^\star$ (`dt`). In the following algorithm upper-index n corresponds to the value of the quantity in certain time $t^{\star(n)}$, where $n = 1,2,...,N_{t^\star}$.

First, radiation field is calculated for each electron at each point of retarded time $t^{\star(n)}$ (implementation is located in `scatteredField.m`). According to the section 3.1, the calculation is performed over retarded time, however, resulting field is expressed in time of the observer $t^{(n)}$.

The algorithm for calculating radiation field has the following computational steps:

1. The distance between the electron and an observer:

$$R^{(n)} = \sqrt{\left(x - r_x^{(n)}\right)^2 + \left(y - r_y^{(n)}\right)^2 + \left(z - r_z^{(n)}\right)^2}, \tag{4.24}$$

   where $\boldsymbol{x} = (x,y,z)$ is the position of the observer and $\boldsymbol{r}^{(n)} = \left(r_x^{(n)},r_y^{(n)},r_z^{(n)}\right)$ is the position of the electron in time $t^{\star(n)}$. Since the observer is far away from the electron, the unit vector $\boldsymbol{n} = \frac{\boldsymbol{x}}{|\boldsymbol{x}|}$ shall be considered as a constant.

2. Time of the observer:

$$t^{(n)} = t^{\star(n)} + \frac{R^{(n)}}{c}. \tag{4.25}$$

3. Lorentz factor:

$$\gamma^{(n)} = \sqrt{1 + \frac{\left(p_x^{(n)}\right)^2 + \left(p_y^{(n)}\right)^2 + \left(p_z^{(n)}\right)^2}{m_e^2 c^2}}. \tag{4.26}$$

4. Normalized electron velocity:

$$\beta_j^{(n)} = \frac{p_j^{(n)}}{\gamma^{(n)} m_e c}, \qquad j = x,y,z. \tag{4.27}$$

5. Normalized electron acceleration using forward difference method:

$$\alpha_j^{(n+1)} = \frac{\beta_j^{(n+1)} - \beta_j^{(n)}}{\Delta t^{\star}}, \qquad j = x,y,z. \tag{4.28}$$

6. Eventually, radiation field of an electron:

$$\begin{aligned}
E_{Rx}^{(n)} &= \frac{e}{4\pi\varepsilon_0 c} \frac{\mathcal{A}^{(n)}\left(n_x - \beta_x^{(n)}\right) - \left(1 - \mathcal{B}^{(n)}\right)\alpha_x^{(n)}}{\left(1 - \mathcal{B}^{(n)}\right)^3 \cdot R^{(n)}}, \\
E_{Ry}^{(n)} &= \frac{e}{4\pi\varepsilon_0 c} \frac{\mathcal{A}^{(n)}\left(n_y - \beta_y^{(n)}\right) - \left(1 - \mathcal{B}^{(n)}\right)\alpha_y^{(n)}}{\left(1 - \mathcal{B}^{(n)}\right)^3 \cdot R^{(n)}}, \\
E_{Rz}^{(n)} &= \frac{e}{4\pi\varepsilon_0 c} \frac{\mathcal{A}^{(n)}\left(n_z - \beta_z^{(n)}\right) - \left(1 - \mathcal{B}^{(n)}\right)\alpha_z^{(n)}}{\left(1 - \mathcal{B}^{(n)}\right)^3 \cdot R^{(n)}},
\end{aligned} \tag{4.29}$$

   where

$$\begin{aligned}
\mathcal{B}^{(n)} &= n_x\beta_x^{(n)} + n_y\beta_y^{(n)} + n_z\beta_z^{(n)}, \\
\mathcal{A}^{(n)} &= n_x\alpha_x^{(n)} + n_y\alpha_y^{(n)} + n_z\alpha_z^{(n)}.
\end{aligned} \tag{4.30}$$

4.3.2 Spectral intensity of radiation

After the radiation field for each electron is calculated, Fourier transform can be applied, according to equation (4.23), to get the spectral intensity of radiation for a single electron. Radiation spectra for an electron bunch is obtained as the summation over the all single electron spectra. However, this approach is only valid when electrons are randomly distributed inside the bunch. In $\mathcal{COCO}$ simulation, the coherence properties in resulting spectra are sustained first by a summation of radiation fields from all electrons and second by Fourier transform of the total radiation field. The summation of the radiation fields must be performed in the same observer time, however, the vector of the time of the observer differs for each electron, since each electron has different initial momentum and position. Therefore, before summation, radiation field for each electron must be firstly expressed in the same time of the observer.

The algorithm for calculation radiation spectra has following steps:

1. The maximum and minimum value of the time of the observer:

$$\begin{aligned} t_{min} &= \min_{e\in\text{bunch}} t_{min}^{\{e\}}, \\ t_{max} &= \max_{e\in\text{bunch}} t_{max}^{\{e\}}. \end{aligned} \tag{4.31}$$

2. The number of samples necessary to satisfy the Nyquist-Shannon theorem [80]:

$$N_\tau = \frac{\aleph \bar{\mathcal{E}}_m (t_{max} - t_{min})}{\pi\hbar}, \tag{4.32}$$

   where $\bar{\mathcal{E}}_m$ is an expected mean energy of the scattered photons in spectra calculated for an electron bunch according to the equation (2.11). The multiplicative constant $\aleph$ can be set in input file (by default $\aleph = 4$).

3. New time vector $\tau \in (t_{min}, t_{max})$ with N_τ samples is created.

4. Each radiation field is re-sampled with regard to a new time vector τ and added to a total radiation field $\boldsymbol{E}_R^{(\tau)}$. The upper-index (τ) suggests, that the quantity is expressed in the time τ. The distance from the electron bunch to the observer $R^{(\tau)}$ is calculated for each time t as a mean value of $R^{(n)}$ over all electrons and then also re-sampled with regard to a new time vector τ.

5. After that, fast Fourier transform is performed using Matlab function `fft()`. The total spectral intensity of radiation is computed according to the equation (4.23) as

$$\frac{d^2 I}{d\omega d\Omega} = \frac{c\varepsilon_0}{\pi} \frac{\left(\left| \mathfrak{F}[E_{Rx} R^{(\tau)}] \right|^2 + \left| \mathfrak{F}[E_{Ry} R^{(\tau)}] \right|^2 + \left| \mathfrak{F}[E_{Rz} R^{(\tau)}] \right|^2 \right)}{F_s^2}, \tag{4.33}$$

   where $F_s = \bar{\mathcal{E}}_m/(\pi\hbar)$ is sampling frequency and also scaling constant for the Matlab function `fft()`.

4.3.3 Spatial distributions of the radiation

Radiation spectrum is calculated for an observer in the far distance from the source, e.g. $R = 1\,\mathrm{m}$. For an observer with position $\boldsymbol{x}$, electron with the position $\boldsymbol{r}(t)$ seems to be at the origin ($|\boldsymbol{x}| - |\boldsymbol{r}(t)| \simeq |\boldsymbol{x}|$) during the whole time of simulation. Radiation field and spectral intensity can be calculated for any position of the observer. One can define angles φ_P and θ_P according to Fig. 4.4 to describe position of an observer $\boldsymbol{x}$ as follows:

$$\begin{aligned} x &= x \\ y &= x \cdot \tan(\varphi_P) \\ z &= x \cdot \tan(\theta_P) \end{aligned} \tag{4.34}$$

Angles φ_P and θ_P are usually very small ($\sim$ mrad). Angular distributions of the radiation can be obtained, when radiated energy per solid angle is obtained for each position of an observer within a solid angle $\left|\varphi_P^{max} - \varphi_P^{min}\right| \times \left|\theta_P^{max} - \theta_P^{min}\right|$. Radiated energy per solid angle reads

$$\frac{dI}{d\Omega} = \sum_{\omega} \frac{d^2 I}{d\omega d\Omega} d\omega. \tag{4.35}$$

Integration of the quantity $dI/d\Omega$ over the solid angle Ω gives total radiated energy. From this relation, one can get number of emitted photons with a mean energy $\mathcal{E}_m$ as follows

$$N_\gamma = \frac{\sum_\Omega \frac{dI}{d\Omega} d\Omega}{\mathcal{E}_m}. \tag{4.36}$$

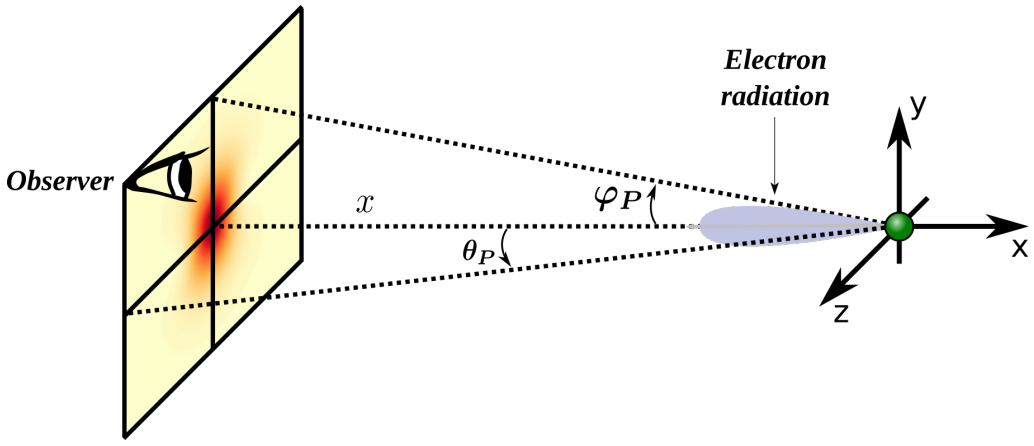

Figure 4.4: An observer is on the plane perpendicular to the propagation direction of the electron in the far distance. Position of the observer can be defined by the angles φ_P and θ_P according to the equations (4.34)

4.3.4 $\mathcal{COCO}$ simulation limits

Using fast Fourier transform brings certain limits. Nyquist–Shannon sampling theorem [80] provides a prescription for the nominal sampling interval required to avoid aliasing when using the FFT. In other words, the sampling frequency for radiation field should be at least twice the highest frequency contained in the spectrum. This is not a problem for a single electron simulation, since electron usually radiates (in observer time) over a few as ($\sim 10^{-18}$ s). On the other hand, this could be a demanding task when electron bunch is simulated. In order to keep coherence properties in resulting spectra, radiation fields from each electron are first summed (Sec. 4.3.2). If electron bunch with high mean energy and large energy spread is considered, this could lead to a relatively long lasting total radiation field, since radiation field from each electron reaches observer in the different time.

Electron bunch typically radiates over a few fs, for example the period $T = 10^{-14}$ s and the highest harmonic component corresponding to the energy $\mathcal{E}_{max} = 10$ MeV is considered. Then the sampling frequency must be at least

$$F_s = 2 \cdot f_{max} = 2 \cdot \frac{\mathcal{E}_{max}}{2\pi\hbar} \simeq 10^{22} \text{ Hz}. \tag{4.37}$$

Thus, for perfectly reconstructed spectra, it is necessary to have at least

$$N = T \cdot F_s \simeq 10^8 \tag{4.38}$$

samples. Working with such number of samples could be difficult.

Furthermore, in $\mathcal{COCO}$ simulation radiation reaction of an electron, thus also electron self-interaction, is neglected. This is valid if the number of oscillations of sub-GeV electron beams in the laser pulse of strength parameter of the order of unity is smaller than 10^3 [74]. In the case of femtosecond laser pulses, this is always fulfilled. Other QED effects, such as electron positron pair production are also neglected.

$\mathcal{COCO}$ simulation focuses mainly on sub-GeV single electron scattering in the field of the laser modeled as a Gaussian beam with strength parameter $a_0 < 20$.

4.4 Single electron $\mathcal{COCO}$ simulation

4.4.1 Electron trajectory

Electron motion in the field of the laser is investigated using $\mathcal{COCO}$ simulation. The trajectory of the electron is numerically calculated according to the algorithm introduced in section 4.2. First, head-on collision is considered. Electron is moving from the origin of the reference frame to the negative direction of the x axis. Laser pulse, described by one of the models from section 4.1.1, is propagating towards the electron in direction of x axis.

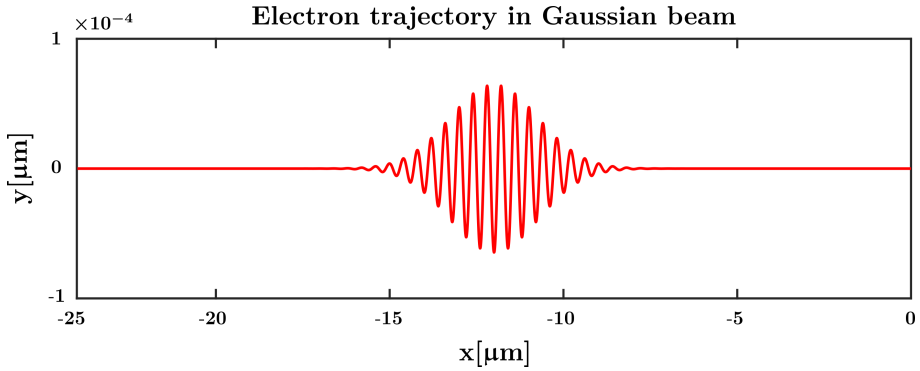

Figure 4.5: Electron with initial energy 102.2 MeV is moving from the origin of the reference frame to the negative direction of the x axis towards the laser. Laser is modeled as a Gaussian beam with $a_0 = 0.2$, $\lambda = 800\,\text{nm}$, FWHM $= 20\,\text{fs}$ and $\sigma_0 = 8.5\,\mu\text{m}$.

For example, the trajectory of an electron with energy 102.2 MeV ($\gamma = 200$) in the field of the laser with strength parameter $a_0 = 0.2$ is depicted in Fig. 4.5. The laser is modeled as a Gaussian beam with Gaussian temporal profile. At the beginning of the simulation, electron was moving straight (to the left) with the velocity given by (1.10). When the intensity of the laser pulse increased, electron started to oscillate transversely in the direction of polarization of the laser. When laser passed, electron continued in its origin direction.

The situation can be different when an electron with relatively low initial energy interacts with relatively high intense laser. For instance, electron trajectories for an electron with initial energy 1.022 MeV ($\gamma = 2$) and three different laser strength parameters are shown in Fig. 4.6. In the case of $a_0 = 2$ (blue curve), electron oscillated similarly as in the previous case, while in the case of $a_0 = 10$ (red curve), electron was delayed in a high intensity region. This was caused due to the $|\boldsymbol{v} \times \boldsymbol{B}|$ part of the Lorentz force (4.12). In the case of ultra intense laser pulse, e.g. $a_0 = 100$ (yellow curve) electron was forced by the $|\boldsymbol{v} \times \boldsymbol{B}|$ force to move to the opposite direction. However, in all cases, the electron continued in its origin direction, when the laser passed.

In other simulation, the typical features of an electron trajectory were investigated. Electron with the initial energy 102.2 MeV was propagating from the origin in the $-\hat{\boldsymbol{x}}$ direction over 40 fs. The counter-propagating laser pulse was modeled as a Gaussian beam with a Gaussian temporal envelope with FWHM $= 20\,\text{fs}$ and the wavelength

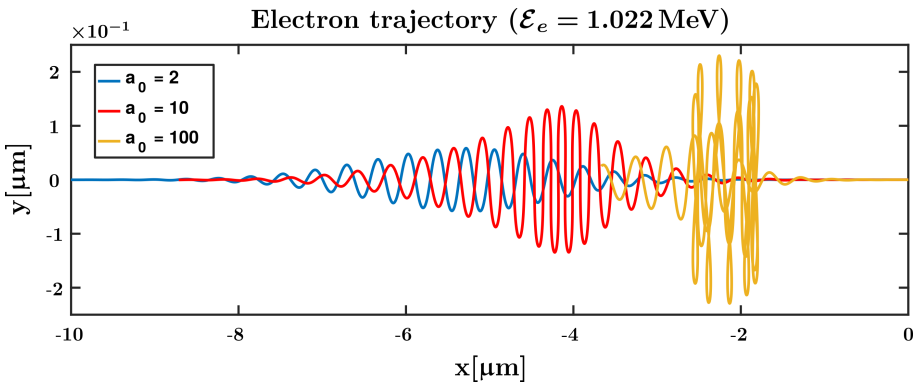

Figure 4.6: Electron with the initial energy 1.022 MeV is moving from the origin of the reference frame to the negative direction of the x axis towards the laser. Laser is modeled as a Gaussian beam with $\lambda = 800\,\mathrm{nm}$, FWHM $= 20\,\mathrm{fs}$ and $\sigma_0 = 8.5$ μm. Three different laser strength parameters: $a_0 = 2$ (blue curve), $a_0 = 10$ (red curve), $a_0 = 100$ (yellow curve).

$\lambda = 0.8\,\mu\mathrm{m}$. Three values of laser strength parameter were used: $a_0 = 0.2$ for linear (undulator) regime, $a_0 = 2$ for mildly non-linear regime and $a_0 = 10$ for non-linear (wiggler) regime. Fig. 4.7 shows orbits of a test electron for each situation. In all cases, the electron has moved approximately $12\,\mu\mathrm{m}$ in the negative direction of x axis and oscillated in y axis with a wavelength $\lambda_e = 0.4\,\mu\mathrm{m}$. This is exactly half of the laser wavelength. The number of electron oscillation periods was the same as a number of optical cycles of the incident laser. The maximal oscillation amplitude differed for each situation. In the linear regime $a_0 = 0.2$ (blue trajectory), the amplitude reached the value $6.44 \cdot 10^{-5}\,\mu\mathrm{m}$. In the case of mildly non-linear regime $a_0 = 2$ (red trajectory) the maximal amplitude was $6.44 \cdot 10^{-4}\,\mu\mathrm{m}$ and for the nonlinear wiggler regime $a_0 = 10$ (yellow trajectory) the amplitude exceeded the value $3.23 \cdot 10^{-3}\,\mu\mathrm{m}$. Theses trajectories are exactly the same as trajectories depicted in the figure 35 in Ref. [74].

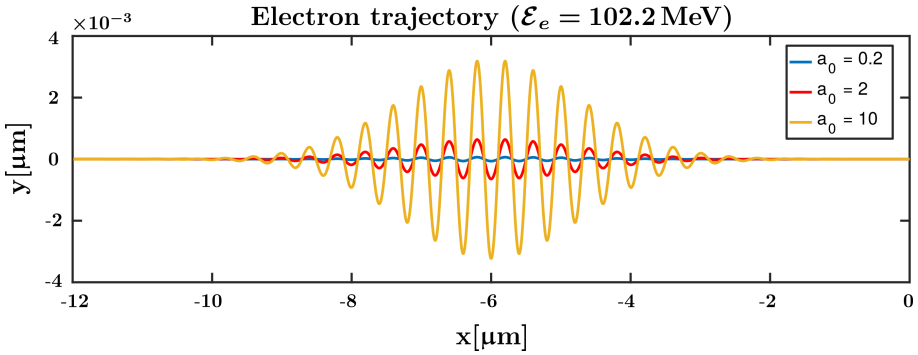

Figure 4.7: Electron with the initial energy 102.2 MeV is moving from the origin of the reference frame to the negative direction of the x axis towards the laser. Laser is modeled as a Gaussian beam with $\lambda = 800\,\mathrm{nm}$, FWHM $= 20\,\mathrm{fs}$ and $\sigma_0 = 8.5$ μm. Three different laser strength parameters: $a_0 = 0.2$ (blue curve), $a_0 = 2$ (red curve), $a_0 = 10$ (yellow curve).

4.4.2 Linear regime (undulator)

Radiation properties, such as spectrum, divergence and the number of emitted photons for the electron in the linear regime of ICS is investigated in this subsection using $\mathcal{COCO}$ simulation. This corresponds to the regime of undulator. According to the section 3.4 the spectrum for this regime consists of a single peak at the fundamental frequency, which can be obtained from the energy of the scattered photon given by the equation (2.11). First, the theoretical analysis of the ICS from section 2.2 and 3.5 is used to test $\mathcal{COCO}$ simulation for the observer on the x axis. Second, a different position of the observer is taken into account and results are compared to the angular distribution of the maximum scattered photon energy. Finally, radiation properties for an electron with the initial energy 102.2 MeV propagating against a laser modeled as a Gaussian beam with a Gaussian temporal profile are discussed. Numerical results obtained by $\mathcal{COCO}$ simulation are also compared to the results published in Ref. [74] for the same initial parameters. In the whole subsection, these parameters of the laser are used: the laser strength parameter $a_0 = 0.2$, the laser wavelength $\lambda_L = 0.8\,\text{nm}$, a pulse duration $FWHM = 20\,\text{fs}$ and a beam waist $\sigma_0 = 8.5\,\mu\text{m}$.

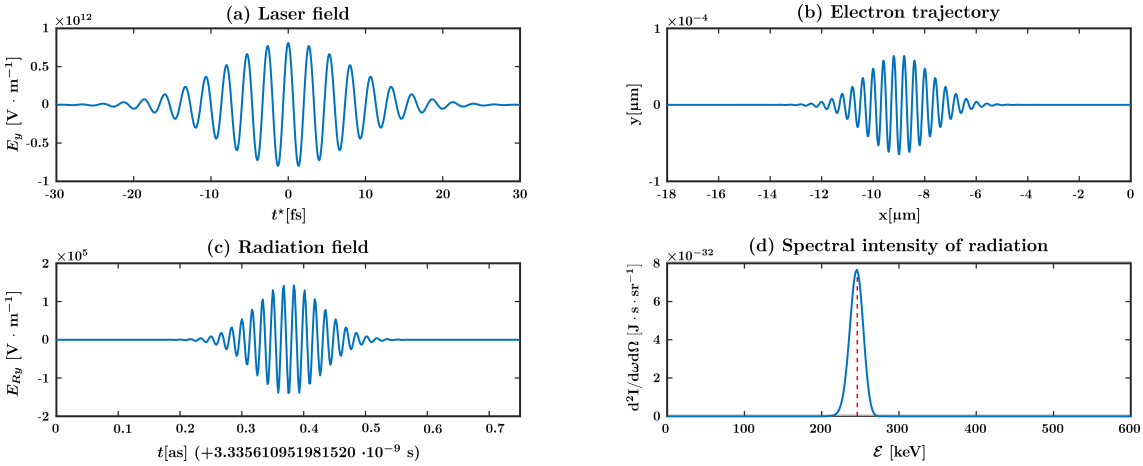

Figure 4.8: Results for the on-axis $\mathcal{COCO}$ simulation in the linear regime ($a_0 = 0.2$). Initial parameters: $\mathcal{E}_e = 102.2\,\text{MeV}$, $\boldsymbol{P} = (-1,0,0)$, $\lambda_L = 0.8\,\text{nm}$, $FWHM = 20\,\text{fs}$, $\sigma_0 = 8.5\,\mu\text{m}$, $t^\star \in (-30\,\text{fs}, 30\,\text{fs})$, $\Delta t = 0.1\,\text{fs}$.

$\mathcal{COCO}$ simulation for an electron with initial energy $\mathcal{E}_e = 102.2\,\text{MeV}$ and the position of the observer $\boldsymbol{P} = (-1,0,0)$ has been launched and corresponding results are depicted in Fig. 4.8. The time evolution of the electric field of the incident laser is plotted in Fig. 4.8a. The simulation started at the time $t_1 = -30\,\text{fs}$ and run over 60 fs with a time step $\Delta t = 0.1\,\text{fs}$. The motion of the electron during the simulation is in Fig. 4.8b. The transverse motion consists of an oscillationin at a period $\lambda_e = 0.4\,\mu\text{m}$ and its amplitude follows the envelope of the laser pulse and increases as the intensity increases. According to this equation [74]

$$\lambda_\gamma = \frac{\lambda_e}{2\gamma^2}\left(1 + \frac{a_0^2}{2} + \gamma^2\vartheta\right), \tag{4.39}$$

the spatial period of the radiation field is approximately $\lambda_R = 5.1\,\text{pm}$. Corresponding time period of the radiation is $T_R = \lambda_R/c = 17.1 \cdot 10^{-3}\,\text{as}$. The time evolution

of the y-component of radiation field is in Fig. 4.8c, where oscillation period is $16.8 \cdot 10^{-3}$ as. This essentially agrees with the estimated value. In the linear regime, the spectrum consists in one single peak at fundamental frequency ($\omega_0 \simeq 2\pi c/\lambda_R$). Indeed, numerically calculated spectra (Fig. 4.8d) shows peak at the photon energy of 246 keV. Theoretically, according to the equation (2.11), energy of the scattered photon is 247 keV (red dashed line in Fig. 4.8d).

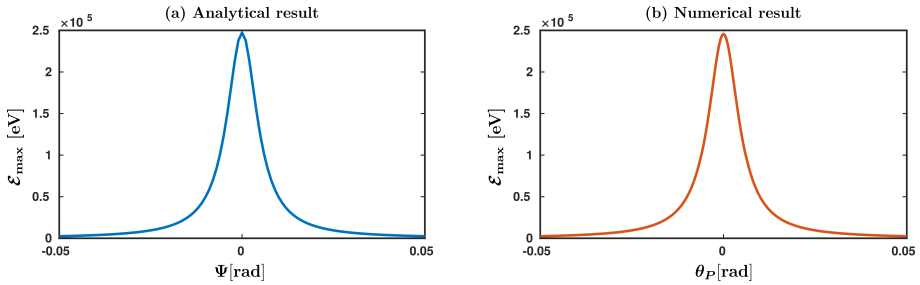

Figure 4.9: (a) the angular distribution of the maximum energy of scattered photons, calculated according the equation (2.11). (b) the dependency of the spectral energy peak upon the observing angle θ_P calculated numerically. Initial parameters: $\mathcal{E}_e = 102.2\,\mathrm{MeV}$, $a_0 = 0.2$, $\lambda_L = 0.8\,\mathrm{nm}$, $FWHM = 20\,\mathrm{fs}$, $\sigma_0 = 8.5\,\mu\mathrm{m}$, $t^\star \in (-30\,\mathrm{fs}, 30\,\mathrm{fs})$, $\Delta t = 0.1\,\mathrm{fs}$.

Equation (2.11) can be also used for testing $\mathcal{COCO}$ simulation for an observer outside the x axis. Analytic calculation of angular distribution of the maximum energy of scattered photons (Fig. 4.9a) gives the same graph as dependency of the spectral energy peak upon the observing angle θ_P, which is the angle between vectors $\boldsymbol{P}$ and $-\hat{\boldsymbol{x}}$ in xz-plane (Fig. 4.9b).

The same simulation ($\mathcal{E}_e = 102.2\,\mathrm{MeV}$) has been launched for a various observation angles. Fig. 4.10a represents calculated spectra of the emitted radiation per unit frequency ($dI/d\omega$), integrated over three selected solid angles $(-1.5{,}1.5)^2$, $(-4{,}4)^2$, $(-10{,}10)^2$ mrad^2. Values on the y axis are expressed in total number of photons within a bandwidth (BW) of 0.1 % of the central energy. In other words

$$\left[\frac{\text{Photons}}{0.1\%\,\text{BW}}\right] = \left[\frac{1}{10^3\hbar}\frac{dI}{d\omega}\right]. \tag{4.40}$$

Calculated spectra using $\mathcal{COCO}$ simulation agrees with results published in Ref. [74] obtained for the same parameters (see Fig. 4.10b). Spectrum is nearly monochromatic at the energy around 247 keV in the forward direction and it is broadened after integration over the emission angles due to the angular dependence of the radiated wavelength given by (4.39). The bandwidth is highly degraded when integrating over the total angular distribution, the critical energy is then $\omega_c \simeq 190\,\mathrm{keV}$.

The spatial distributions of the radiation (radiated energy per unit solid angle) calculated using $\mathcal{COCO}$ simulation is depicted in Fig. 4.11. The picture is the same as the one, obtained for the same parameters in Ref. [74] (see Fig. 4.10b). The radiation has a divergence of typical opening angle $\vartheta = 1/\gamma \sim 5\,\mathrm{mrad}$, which agrees with theoretical review of an undulator regime in section 3.3. The highest radiated energy is for on-axis configuration (observing angles $\theta_P = \varphi_P = 0\,\mathrm{rad}$) at the value $2.525 \cdot 10^{-12}\,\mathrm{J \cdot sr^{-1}}$.

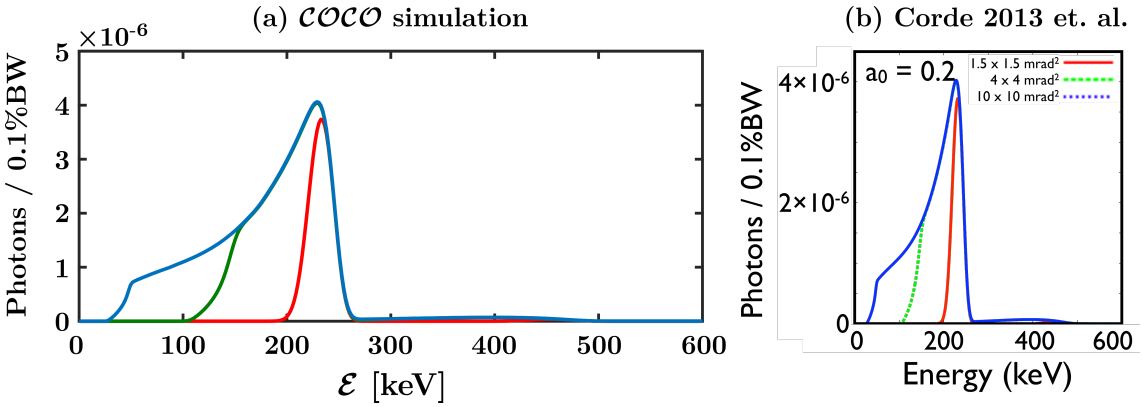

Figure 4.10: Total spectra of the emitted radiation per unit frequency for linear regime ($a_0 = 0.2$). (a) *COCO* simulation. (b) Results from Ref. [74]. Integration has been performed over three selected solid angles $(-1.5,1.5)^2$ mrad^2 (red curve), $(-4,4)^2$ mrad^2 (green curve), $(-10,10)^2$ mrad^2 (blue curve). Initial parameters: $\mathcal{E}_e = 102.2\,\text{MeV}$, $a_0 = 0.2$, $\lambda_L = 0.8\,\text{nm}$, $FWHM = 20\,\text{fs}$, $\sigma_0 = 8.5\,\mu\text{m}$, $t^\star \in (-30\,\text{fs},30\,\text{fs})$, $\Delta t = 0.1\,\text{fs}$.

The total radiated energy can be calculated either by the integration of total spectra (Fig. 4.10) over the energy or by integrating the radiated energy per solid angle over the total angular distribution (Fig. 4.11):

$$\mathcal{E}_{\text{total}} = \sum_{\omega} \frac{dI}{d\omega} d\omega = \sum_{\Omega} \frac{dI}{d\Omega} d\Omega. \tag{4.41}$$

In both cases the total radiated energy yields $\mathcal{E}_{\text{total}} = 6.8749 \cdot 10^{-17}\,\text{J}$, which corresponds to the total number of $2.3 \cdot 10^{-3}$ emitted photons with critical energy 190 keV per electron per shot. The estimate for this value for $a_0 \ll 1$ is given by the equation (3.22). It yields $6.1 \cdot 10^{-3}$ emitted photons per electron per shot, considering approximately 10 electron oscillation periods in the FWHM laser pulse duration of 20 fs.

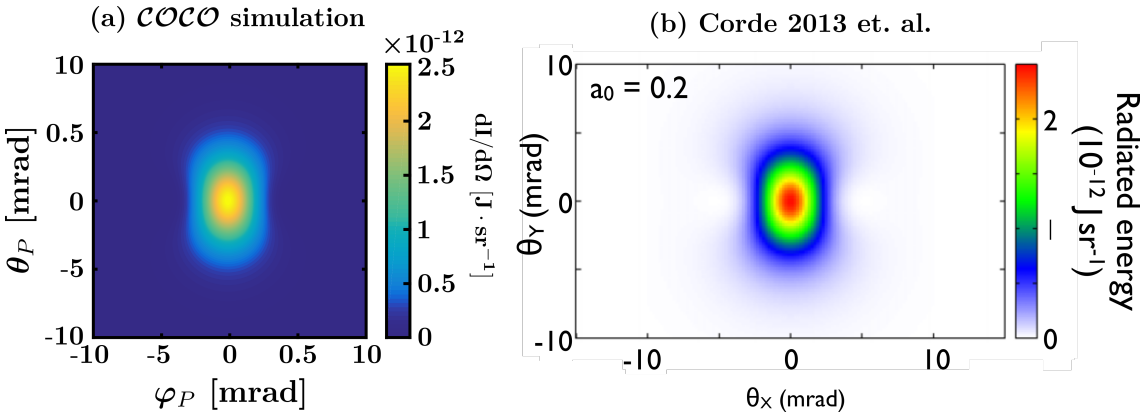

Figure 4.11: The spatial distribution of the radiation for linear regime ($a_0 = 0.2$). (a) *COCO* simulation. (b) Results from Ref. [74]. Initial parameters: $\mathcal{E}_e = 102.2\,\text{MeV}$, $\lambda_L = 0.8\,\text{nm}$, $FWHM = 20\,\text{fs}$, $\sigma_0 = 8.5\,\mu\text{m}$, $t^\star \in (-20\,\text{fs},20\,\text{fs})$, $\Delta t = 0.1\,\text{fs}$.

4.4.3 Mildly nonlinear regime

Inverse Compton scattering using laser with a strength parameter $1 < a_0 < 5$ is investigated in this subsection. This cannot be classified as a pure undulator regime nor wiggler regime. However, according to the section 3.3, it is closer to the wiggler regime, since $a_0 > 1$ and electron radiates in the different sections of the trajectory in different directions. The spectrum is no longer monochromatic, but contains many harmonics. For better understanding of this behavior, on-axis radiation is presented for both an electromagnetic plane-wave and a Gaussian beam. Then, radiation properties for an electron with initial energy 102.2 MeV propagating against laser modeled as a Gaussian beam with a Gaussian temporal profile are discussed. Numerical results obtained by $\mathcal{COCO}$ simulation are also compared to the results published in Ref. [74] for the same initial parameters. In the whole subsection, these parameters remain unchanged: the laser strength parameter $a_0 = 2$, the laser wavelength $\lambda_L = 0.8\,\text{nm}$, the pulse duration $FWHM = 20\,\text{fs}$, the beam waist $\sigma_0 = 8.5\,\mu\text{m}$ and the electron initial energy $\mathcal{E}_e = 102\,\text{MeV}$.

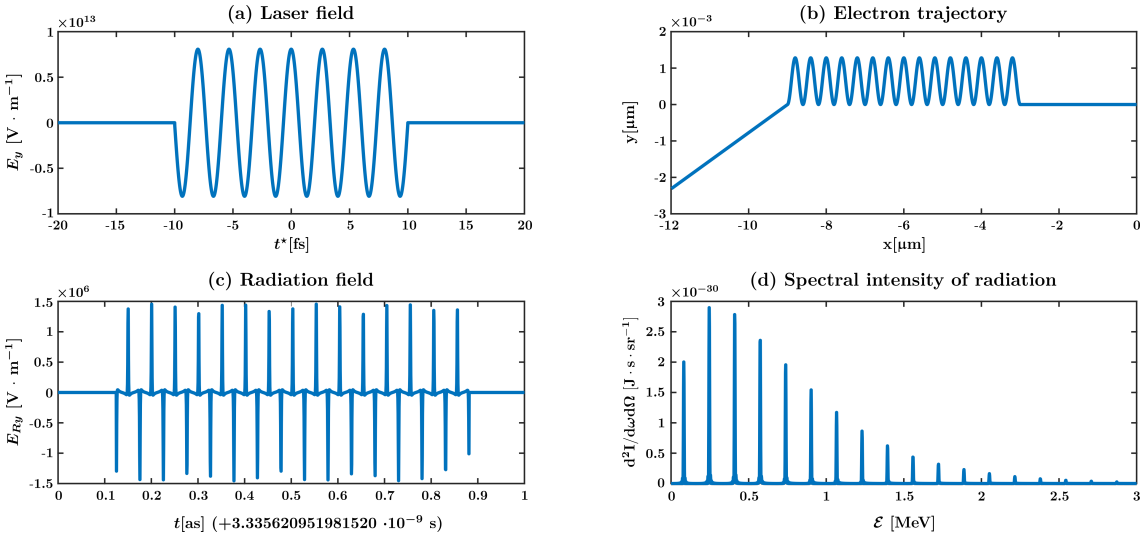

Figure 4.12: Results for the on-axis $\mathcal{COCO}$ simulation in a mildly nonlinear regime ($a_0 = 2$). The laser is modeled as a time-limited electromagnetic plane wave with a rectangular temporal profile. Initial parameters: $\mathcal{E}_e = 102.2\,\text{MeV}$, $\boldsymbol{P} = (-1,0,0)$, $\lambda_L = 0.8\,\text{nm}$, $FWHM = 20\,\text{fs}$, $t^\star \in (-20\,\text{fs}, 20\,\text{fs})$, $\Delta t = 0.1\,\text{fs}$.

First, the laser is modeled as a time-limited electromagnetic plane wave with a rectangular temporal profile. In other words, it is an electromagnetic plane wave, which lasts only for a limited time, set to value $FWHM$. The time evolution of the electric field of the incident laser is depicted in Fig. 4.12a. The simulation started at the time $t_1 = -20\,\text{fs}$ and run over 40 fs with a time step $\Delta t = 0.1\,\text{fs}$. Electron is initially moving in the negative direction of the x axis towards the laser (Fig. 4.12b). When the laser is switched on, electron starts to oscillate with a maximum amplitude $6.05 \cdot 10^{-4}\,\mu\text{m}$ around the point $y = 6.05 \cdot 10^{-4}\,\mu\text{m}$. At the end of the interaction electron continues straight with a such momentum, which electron gains, when the laser was switched off. This last part of the trajectory has no influence on the resulting spectra, since there is no electron acceleration. The time evolution of the y-component of radiation field and corresponding spectra for an observer at the

position $\boldsymbol{P} = (-1,0,0)$ is in Fig. 4.12c-d. As expected, spectra does not contain single peak as in the case of on-axis linear regime. In addition to the fundamental energy $\mathcal{E}_1 \simeq 82\,\mathrm{keV}$, higher harmonics of shorter wavelength, $\lambda_n = \lambda_1/n$, are emitted. Their number and intensity increases with a_0. As usual for synchrotron-like spectra, in the case of on-axis radiation ($\varphi_P = \theta_P = 0$) only odd harmonics are emitted. Also the spectral envelope reminds sychrotron spectrum.

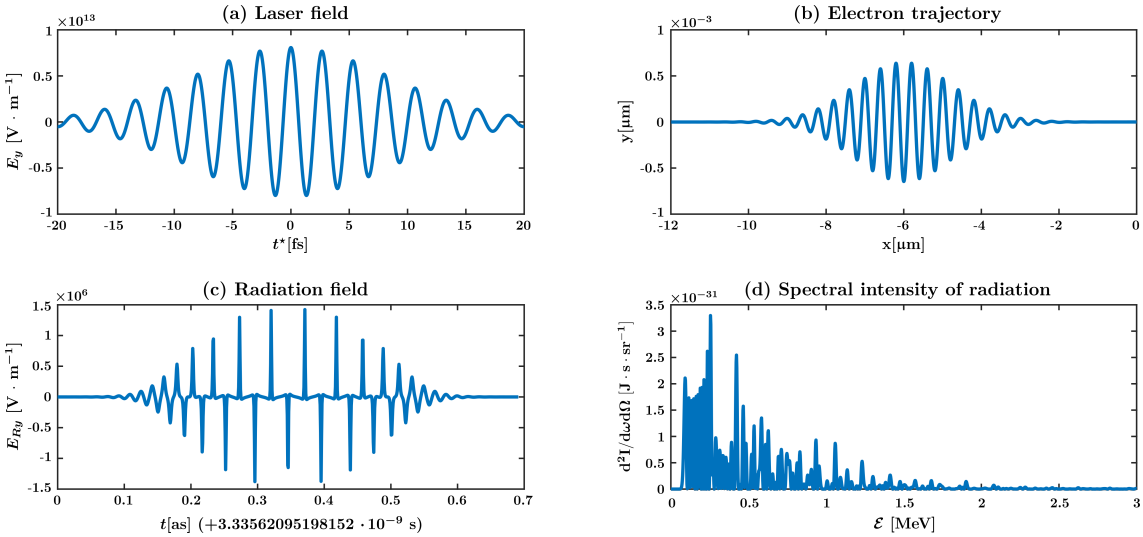

Figure 4.13: Results for the on-axis $\mathcal{COCO}$ simulation in a mildly nonlinear regime ($a_0 = 2$). The laser is modeled as a Gaussian beam with Gaussian temporal profile. Initial parameters: $\mathcal{E}_e = 102.2\,\mathrm{MeV}$, $\boldsymbol{P} = (-1,0,0)$, $\lambda_L = 0.8\,\mathrm{nm}$, $FWHM = 20\,\mathrm{fs}$, $\sigma_0 = 8.5\,\mu\mathrm{m}$, $t^\star \in (-20\,\mathrm{fs}, 20\,\mathrm{fs})$, $\Delta t = 0.1\,\mathrm{fs}$.

The second simulation has been launched with a laser modeled as a Gaussian beam with a Gaussian temporal profile. The rest parameters remain unchanged as in the previous case. Results of this simulation are shown in Fig. 4.13. Compared to the first simulation, here the electron oscillation amplitude increases slowly as it follows the envelope of the laser pulse. Similar shape can be find for radiation field. This slowly varying envelope of the radiation field with a more complex shapes of oscillations (Fig. 4.13c) results in more complicated radiation spectra (Fig. 4.13d) with a 10 times lower maximal spectral intensity of radiation then in the case of electromagnetic plane wave. However, spectra obtained from both simulations shows the harmonics with an energy up to 2 MeV.

The same initial parameters as in the second simulation (the case of Gaussian beam) are kept and the spectra is calculated for different observation angles. The total radiated energy per unit frequency can be obtained by integrating spectral intensity of radiation over the total angular distribution. Fig. 4.14a represents the total spectrum integrated over $(-15,15)^2$ mrad^2 computed by $\mathcal{COCO}$ simulation. Fig 4.14b shows the same results obtained for the same intital parameters in Ref. [74]. When integrating over the total angular distribution, harmonics overlap and the radiation spectrum becomes continuous, but keeps the same extension up to 2 MeV. The critical energy has been numerically calculated to the value $\mathcal{E}_c = 292.81\,\mathrm{keV}$.

The spatial distribution of the radiation (the radiated energy per unit solid angle) has been also obtained. $\mathcal{COCO}$ simulation result (Fig. 4.15a) again corresponds to the result from Ref. [74] (Fig. 4.15b). As it was suggested in the section 3.3, when

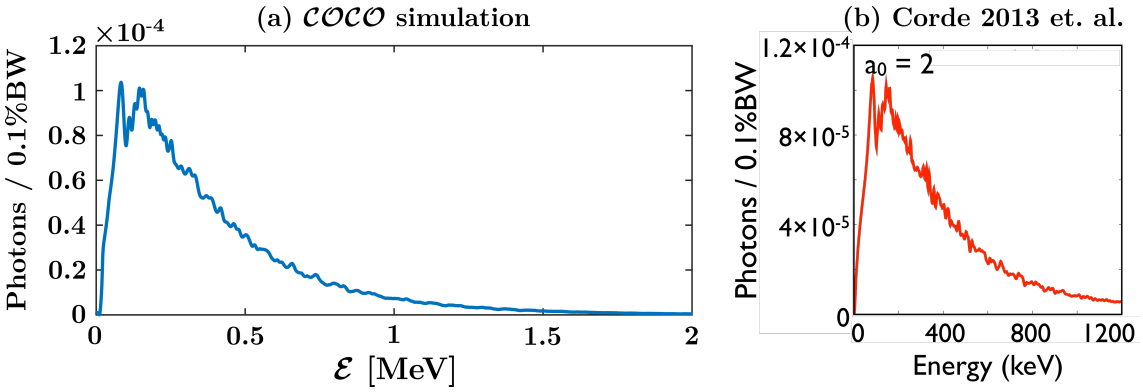

Figure 4.14: Total spectra of the emitted radiation per unit frequency integrated over solid angle $(-15{,}15)^2$ mrad^2 for mindly nonlinear regime ($a_0 = 2$). (a) $\mathcal{COCO}$ simulation. (b) Results from Ref. [74]. Initial parameters: $\mathcal{E}_e = 102.2\,\mathrm{MeV}$, $\lambda_L = 0.8\,\mathrm{nm}$, $FWHM = 20\,\mathrm{fs}$, $\sigma_0 = 8.5\,\mu\mathrm{m}$, $t^\star \in (-20\,\mathrm{fs}{,}20\,\mathrm{fs})$, $\Delta t = 0.1\,\mathrm{fs}$.

$a_0 > 1$ the radiation has a divergence of typical opening angle $\varphi_P \sim a_0/\gamma$ (10 mrad) in the plane of the electron motion and $\theta_P \sim 1/\gamma$ (5 mrad) in the orthogonal direction. The highest radiated energy is for on-axis configuration (observing angles $\theta_P = \varphi_P = 0\,\mathrm{rad}$) at the value $7.49 \cdot 10^{-11}\,\mathrm{J \cdot sr^{-1}}$, which is almost 30 times higher than in the case of linear regime.

The total radiated energy is calculated similarly as in the linear regime according to the equation (4.41). $\mathcal{E}_{\mathrm{total}} = 6.8562 \cdot 10^{-15}\,\mathrm{J}$, which is almost exactly 100 times higher radiated energy then in the case of $a_0 = 0.2$. This is an expected value, because

$$\frac{d^2 I}{d\omega d\Omega} \sim |\boldsymbol{E_R}|^2 \sim a_0^2. \tag{4.42}$$

In the mildly nonlinear regime the total number of 0.49 photons with a peak energy $0.3\mathcal{E}_c = 87\,\mathrm{keV}$ has been emitted per electron per shot.

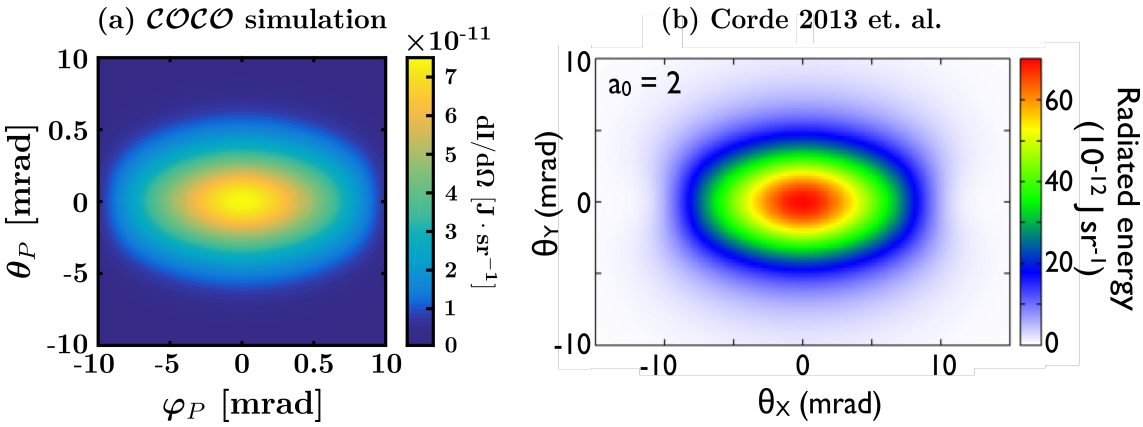

Figure 4.15: The spatial distribution of the radiation for mindly nonlinear regime ($a_0 = 2$). (a) $\mathcal{COCO}$ simulation. (b) Results from Ref. [74]. Initial parameters: $\mathcal{E}_e = 102.2\,\mathrm{MeV}$, $\lambda_L = 0.8\,\mathrm{nm}$, $FWHM = 20\,\mathrm{fs}$, $\sigma_0 = 8.5\,\mu\mathrm{m}$, $t^\star \in (-20\,\mathrm{fs}{,}20\,\mathrm{fs})$, $\Delta t = 0.1\,\mathrm{fs}$.

4.4.4 Nonlinear regime (wiggler)

With the increasing value of the laser strength parameter a_0 the electromagnetic wave of the laser acts as a wiggler. The radiation contains a large number of harmonics, which creates almost continuous spectrum even for on-axis configuration. In the wiggler regime, the spectra of radiation over the total angular distribution becomes synchrotron-like and model of synchrotron radiation given by equation (3.20) can be used in order to test $\mathcal{COCO}$ simulation for a wiggler regime. The laser strength parameter $a_0 = 10$ is used throughout this subsection. This corresponds to laser intensity $I = 2.16 \cdot 10^{20}\,\mathrm{W \cdot cm^{-2}}$ (for $\lambda_L = 0.8\,\mathrm{nm}$). The other laser parameters remain the same as in the previous section: the laser model described as a Gaussian beam with Gaussian temporal profile, the laser wavelength $\lambda_L = 0.8\,\mathrm{nm}$, the pulse duration $FWHM = 20\,\mathrm{fs}$ and the beam waist $\sigma_0 = 8.5\,\mu\mathrm{m}$.

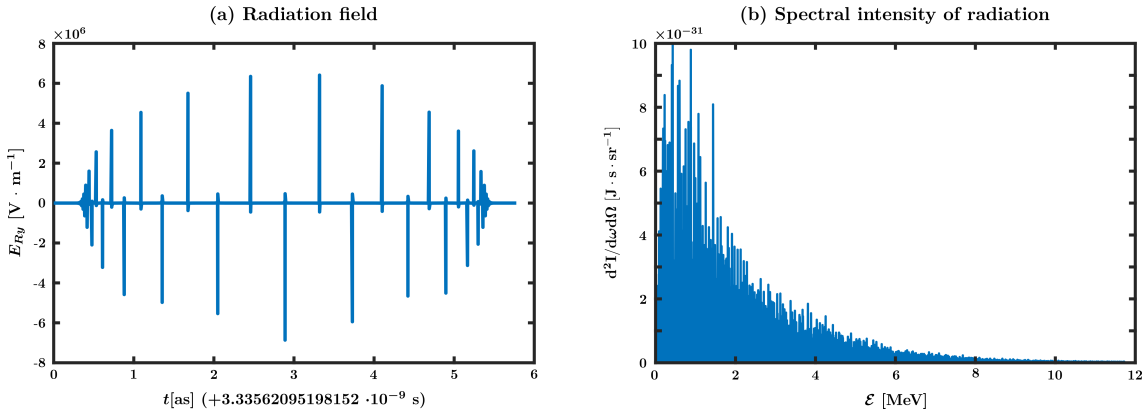

Figure 4.16: Results for the on-axis $\mathcal{COCO}$ simulation in the nonlinear regime ($a_0 = 10$). The laser is modeled as a Gaussian beam with Gaussian temporal profile. Initial parameters: $\mathcal{E}_e = 102.2\,\mathrm{MeV}$, $\boldsymbol{P} = (-1,0,0)$, $\lambda_L = 0.8\,\mathrm{nm}$, $FWHM = 20\,\mathrm{fs}$, $\sigma_0 = 8.5\,\mu\mathrm{m}$, $t^\star \in (-20\,\mathrm{fs}, 20\,\mathrm{fs})$, $\Delta t = 0.1\,\mathrm{fs}$.

Electron with the initial energy $\mathcal{E}_e = 102.2\,\mathrm{MeV}$ again propagates from the origin of reference frame in the negative direction of x axis towards the laser. The trajectory of the electron looks similar as in both previous regimes (see Fig. 4.7), only the oscillation amplitude differs. Here, the maximum amplitude is at the value $3.23 \cdot 10^{-3}\,\mu\mathrm{m}$. Fig. 4.16 shows the radiation field of the electron and the corresponding spectrum for the observer on the x axis at the distance of 1 m from the electron ($\boldsymbol{P} = (-1,0,0)$). In the linear regime, radiation field (Fig. 4.8c) follows the electron oscillations, while in the wiggler regime (Fig. 4.16a) the shape of the radiation field envelope has rather cosine shape than Gaussian. Sharp single peaks in the radiation field results in a large number of harmonics in spectra (Fig. 4.16b). The critical energy for the on-axis radiation has been calculated numerically at the value 1.78 MeV.

Fig. 4.17a (blue curve) represents the total spectrum as a radiated energy per unit frequency (integrated over solid angle $(-50,50)^2$ mrad^2). High harmonics components extends up to 10 MeV. In order to test our simulation, electron trajectory computed by $\mathcal{COCO}$ simulation has been also used to calculate synchrotron spectrum according to equation (3.20). The result is plotted in Fig. 4.17a (red curve). Both graphs are almost identical and overlaps from the energy of 2 MeV. The critical energy of the total spectra is $\mathcal{E}_c = 1.17\,\mathrm{MeV}$. Due to the integration over the solid

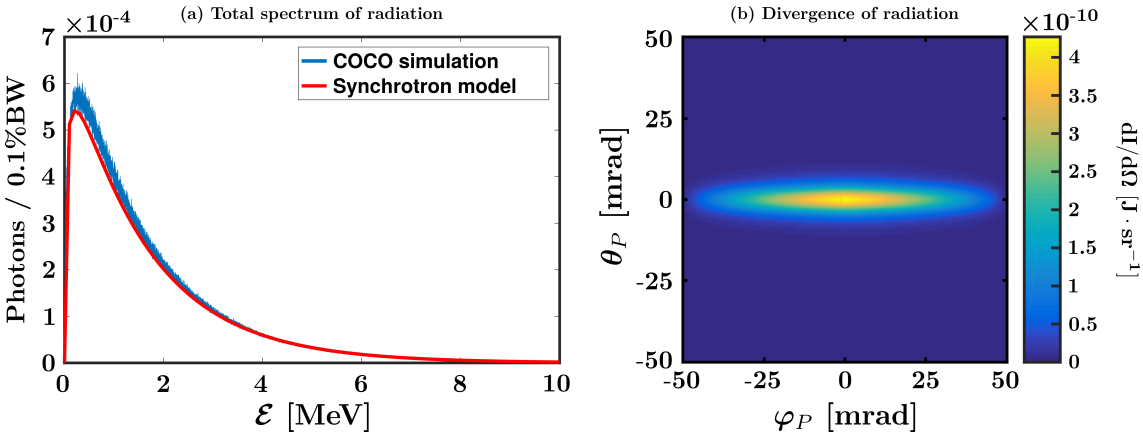

Figure 4.17: (a) Total spectrum of the emitted radiation per unit frequency integrated over solid angle $(-50{,}50)^2$ mrad^2 for nonlinear regime ($a_0 = 10$). (b) The spatial distribution of the radiation for nonlinear regime ($a_0 = 10$). Initial parameters: $\mathcal{E}_e = 102.2\,\mathrm{MeV}$, $\lambda_L = 0.8\,\mathrm{nm}$, $FWHM = 20\,\mathrm{fs}$, $\sigma_0 = 8.5\,\mu\mathrm{m}$, $t^\star \in (-20\,\mathrm{fs}{,}20\,\mathrm{fs})$, $\Delta t = 0.1\,\mathrm{fs}$.

angle, it is smaller than in the case of on-axis radiation. The peak energy is around 353 keV $= 0.3\mathcal{E}_\mathrm{c}$. The spatial distribution of the radiation is presented in Fig 4.17b. The radiation is collimated within a typical opening angle $\varphi_P \sim a_0/\gamma$ (50 mrad) in the electron motion plane and $\theta_P \sim 1/\gamma$ (5 mrad) in the orthogonal plane. In the forward direction ($\theta_P = \varphi_P = 0\,\mathrm{rad}$) electron radiates with the highest energy $4.16 \cdot 10^{-10}\,\mathrm{J \cdot sr^{-1}}$. The total radiated energy yields $\mathcal{E}_\mathrm{total} = 1.8 \cdot 10^{-13}\,\mathrm{J}$, which corresponds to the total number of 3.18 photons with a peak energy $0.3\mathcal{E}_c = 353\,\mathrm{keV}$ per electron per shot. The analytical estimate of this value for $a_0 \gg 1$ is given by the equation (3.24). It yields 3.31 emitted photons per electron per shot, considering approximately 10 electron oscillation periods in the FWHM laser pulse duration of 20 fs.

4.5 Electron bunch $\mathcal{COCO}$ simulation

Since radiation generated by Compton sources are basically incoherent, in most cases single electron simulation is sufficient to investigate radiation properties, such as spectrum, divergence and the number of emitted photons. On the other hand, energy distribution of electrons in bunch can significantly broaden shape of the spectra in linear regime even in the case of on-axis configuration. Therefore, the comparison between the the on-axis spectra for single electron and an electron bunch consists of 10^4 electrons is presented here. Furthermore, the microbunch can be simulated using $\mathcal{COCO}$ simulation to demonstrate significance of the coherence properties of the radiation. In the whole section, these parameters are fixed: the laser wavelength $\lambda_L = 0.8\,\mathrm{nm}$, the pulse duration $FWHM = 20\,\mathrm{fs}$, the beam waist $\sigma_0 = 8.5\,\mu\mathrm{m}$. The laser was modeled as a Gaussian beam with a Gaussian temporal profile.

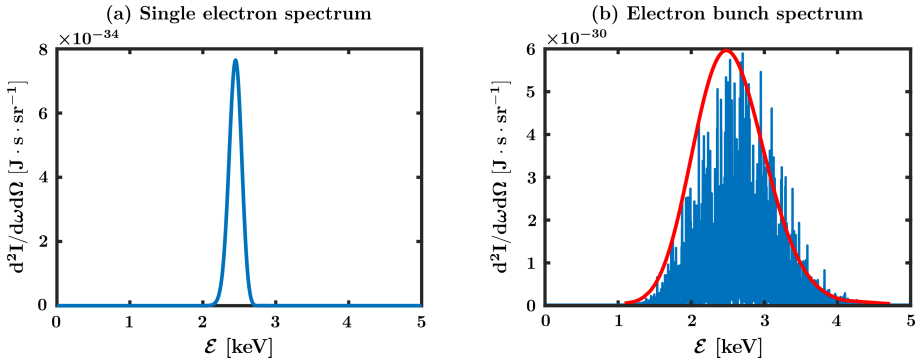

Figure 4.18: On-axis radiation spectrum for linear regime ($a_0 = 0.2$): (a) radiation spectrum for a single electron with the initial energy $\mathcal{E}_e = 10.2\,\mathrm{MeV}$. (b) spectrum of an electron bunch with 10^4 electrons with energies $\mathcal{E}_e$ normally distributed around a mean electron energy $\mathcal{E}_m = 10.2\,\mathrm{MeV}$ with standard deviation $\mathcal{E}_\sigma = 1$ MeV.

Electron bunch consists of 10^4 electrons randomly distributed in the square in the plane of laser polarization with the center at the origin and size of $0.8\,\mu\mathrm{m}$ is considered. Electrons in the bunch has energies $\mathcal{E}_e$ normally distributed around a mean electron energy $\mathcal{E}_e = 10.2\,\mathrm{MeV}$ with standard deviation $\mathcal{E}_\sigma = 1$ MeV. The following simulation started at the time $t_1 = -60\,\mathrm{fs}$ and run over $120\,\mathrm{fs}$ with a time step $\Delta t = 0.1\,\mathrm{fs}$. Two different regimes were investigated. Fig. 4.18 represents on-axis radiation spectra for linear regime ($a_0 = 0.2$). Vertical axis indicates radiated energy per unit solid angle per unit frequency. While single electron spectrum (Fig. 4.18a) consists of one peak at the value of $2.46\,\mathrm{keV}$, spectrum for an electron bunch is broadened (Fig. 4.18b). The estimation of this spectral shape can be obtained by the application of the equation (2.11) on the initial electron energy distribution. This is plotted by a red curve in Fig. 4.18b. For the most part, the calculated spectral shape is located within this estimated curve. The maximum value of the spectral intensity of radiation in the case of electron bunch is approximately 10^4 higher than in the case of single electron. This corresponds to the number of electrons in the bunch. One can get total radiated energy per solid angle by integrating the spectrum over the energy. For the single electron, it yields $2.52 \cdot 10^{-16}\mathrm{J} \cdot \mathrm{sr}^{-1}$, while for the electron bunch, it yields $2.48 \cdot 10^{-12}\mathrm{J} \cdot \mathrm{sr}^{-1}$. This is again approximately 10^4 times higher than in the case of single electron. On-axis radiation spectra for mildly nonlinear regime ($a_0 = 2$) are depicted in Fig. 4.19a for single electron and in Fig. 4.19b

for electron bunch with the same parameters as in the previous simulation. Since $a_0 > 1$, both spectra contains high harmonics, however, the amount of harmonics components is larger in the case of electron bunch due to the initial electron energy distribution. While the critical energy is in both cases approximately the same (around 4.15 keV), to total radiated energy per solid angle differs by four orders. More precisely, for electron bunch it yields $7.88{\cdot}10^{-11}\mathrm{J}\cdot\mathrm{sr}^{-1}$, while for single electron it yields $7.51\cdot10^{-15}\mathrm{J}\cdot\mathrm{sr}^{-1}$.

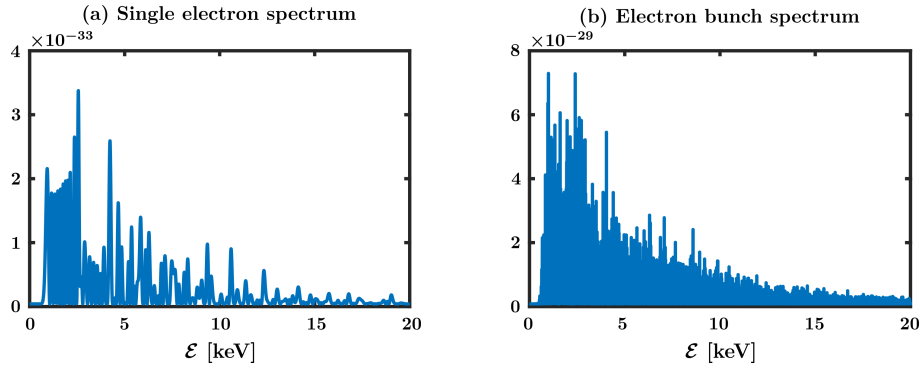

Figure 4.19: On-axis radiation spectrum for mildly non-linear regime ($a_0 = 2$): (a) radiation spectrum for a single electron with the initial energy $\mathcal{E}_e = 10.2\,\mathrm{MeV}$. (b) spectrum of an electron bunch with 10^4 electrons with energies $\mathcal{E}_e$ normally distributed around a mean electron energy $\mathcal{E}_m = 10.2\,\mathrm{MeV}$ with standard deviation $\mathcal{E}_\sigma = 1$ MeV.

Generally spectral properties, such as the shape and divergence remains approximately the same for an electron bunch as for a single electron. Radiated energy, as well as the number of emitted photons for an electron bunch equals to the value of single electron multiplied by the number of electrons in the bunch. However, this is valid for incoherent radiation sources, such as ICS, where electrons are randomly distributed in the bunch. On the other hand, the radiation is orders of magnitude higher, when the electron microbunching is considered. Three different simulation has been launched to demonstrate this phenomena. First, radiated spectra was calculated for a single electron with the initial energy 10.2 MeV (Fig. 4.20a). Second, the same simulation was performed for 10 electrons randomly distributed within a square bunch with the same initial configuration as electron bunches in previous simulations. Corresponding spectrum is depicted in Fig. 4.20b. Third, Fig. 4.20c shows radiated spectrum for the microbunch consists of 10 electrons with the same initial energy 10.2 MeV located at the same position.

All spectra has similar shape and are represented as a radiated energy per unit frequency (integrated over solid angle $(-100{,}100)^2$ mrad^2). The total radiated energy for each case are in table 4.1. Electron bunch with 10 randomly distributed electrons radiates almost exactly 10 times more energy than the single electron. The total radiated energy in the case of microbunch is 100 times higher than in the case of the single electron. According to the section 3.5, this is due to the fact that the radiation from each electron within a microbunch is coherently summed. Resulting total radiated energy is according to equation (3.5) equal to the value of the total radiated energy of a single electron multiplied by the squared power of the number of electrons in the microbunch.

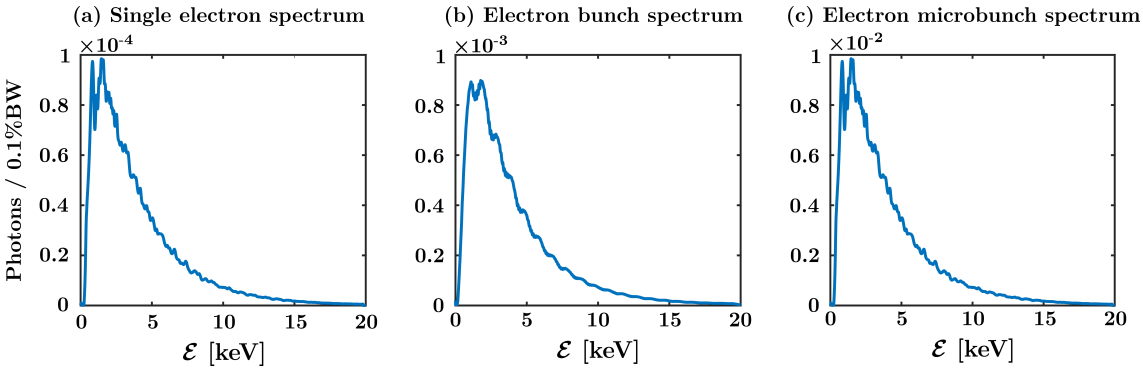

Figure 4.20: Comparison of total spectra of radiation for: (a) single electron with initial energy 10.2 MeV, (b) electron bunch with 10 randomly distributed electrons with energies normally distributed around a mean energy $\mathcal{E}_e = 10.2\,\text{MeV}$ with standard deviation $\mathcal{E}_\sigma = 1$ MeV, (c) electron microbunch with 10 electrons with the same initial energy 10.2 MeV located at the same position.

Type of simulation	Total radiated energy [J]
Single electron	$6.56 \cdot 10^{-17}$
Electron bunch	$6.55 \cdot 10^{-16}$
Electron microbunch	$6.56 \cdot 10^{-15}$

Table 4.1: Comparison of the total radiated energy for three different simulations.

The spatial distribution of radiation for all three cases is depicted in Fig. 4.21. Whereas the divergence is the same for each case, the total radiated energy per solid angle again demonstrate coherence properties of microbunch, where the values of energy are 100 times higher than in the case of a single electron. Special devices for the generation of intense coherent X-ray radiation such as free electron lasers are based on this phenomenom [74].

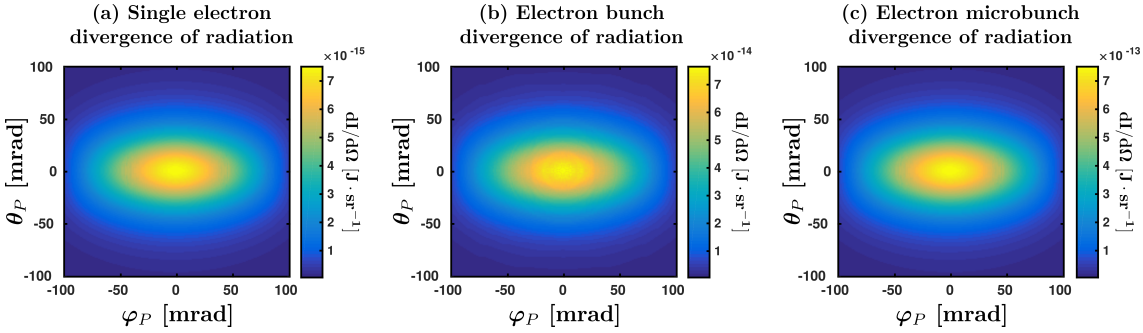

Figure 4.21: Comparison of the spatial distribution of radiation for: (a) single electron with initial energy 10.2 MeV, (b) electron bunch with 10 randomly distributed electrons with energies normally distributed around a mean energy $\mathcal{E}_e = 10.2\,\text{MeV}$ with standard deviation $\mathcal{E}_\sigma = 1$ MeV, (c) electron microbunch with 10 electrons with the same initial energy 10.2 MeV located at the same position.

Conclusion

New and relatively fast *Compton code* ($\mathcal{COCO}$) for calculating radiation properties of inverse Compton scattering (ICS) has been implemented by the author in the program Matlab. Electron trajectories in the field of Gaussian beam were numerically calculated using the 4th order Runge-Kutta scheme. From the trajectories, Liénard–Wiechert potentials were computed at the position of the observer. In order to save computer memory as well as keep coherence properties in resulting radiation, radiated fields from each electron were first summed and then through the use of fast Fourier transform techniques, the spectrum was computed.

$\mathcal{COCO}$ was tested in three different regimes according to the value of the laser strength parameter a_0. Calculated trajectories, radiation spectra and spatial distribution of radiation agreed with corresponding results from the scientific literature. In the linear regime calculated peak energy differed from the estimated value by less than 0.5%. In the case of a nonlinear regime, calculated spectrum agreed with the model of synchrotron radiation, however, $\mathcal{COCO}$ also allowed computing spectrum at the different observing angles.

It was also demonstrated that the spectral shape and divergence remains approximately the same for an electron bunch as for a single electron. However, in the case of a linear regime, a spectrum can be broadened due to the energy distribution of electrons within a bunch. In addition to this, the mechanism of the all-optical free-electron laser based on the ICS was described using $\mathcal{COCO}$ simulation. The electron bunch with 10 randomly distributed electrons radiated approximately 10 times less than the electron microbunch with 10 electrons at the same position.

The limitations of the $\mathcal{COCO}$ simulations were also presented. Since $\mathcal{COCO}$ is based on the Fourier transform, the Nyquist-Shannon sampling theorem must be taken into account. This could be a problem for an electron bunch with high mean energy and large energy spread interacting with high intense laser pulses. Furthermore, in $\mathcal{COCO}$ simulations, QED effects, such as radiation reaction of an electron are also neglected. Therefore, $\mathcal{COCO}$ simulations focus mainly on sub-GeV single electron scattering in the field of the laser with the strength parameter $a_0 < 20$.

Future work will focus on overcoming these limitations and optimization of the algorithm. In conclusion, $\mathcal{COCO}$ is relatively fast in the case of a single electron simulation, therefore, it could be useful tool during the upcoming ICS experiments in the Prague Asterix Laser System facility or in the international project ELI-beamlines.

Appendix A

COCO simulation package description

Here the structure of *COCO* simulation package, which is located on the attached CD is presented. A short description of each script is also given. The *COCO* simulation package is located in the main folder `COCO5` and consists of following folders and scripts:

- `coco.m` - the main simulation script lunched from input file.
- `inputdecks/` - examples of input files.
  - `inputdeck_single.m` - an example of the input file for the single spectrum for an observer at a certain position.
  - `inputdeck_full.m` - an example of the input file for the total spectrum integrated over solid angle.
  - `inputdeck_div.m` - an example of the input file for the spatial distribution of radiation over solid angle.
  - `inputdeck_bunch.m` - an example of the input file for the electron bunch spectrum for an observer at a certain position.
- `working/` - auxiliary scripts.
  - `importConstants.m` - the initialization of physical and simulation constants.
  - `numberOfCPU.m` - starts Matlab parallel computing pool with a number of workers given in the input file.
  - `calculateDerivedQuantities.m` - calculates derived physical quantities from initial parameters given in input file.
  - `clearAllButInputdeck.m` - clear all calculated variables after a simulation (initial parameters are not deleted).
  - `mysave.m` - script for saving figures.

- `laser/` - scripts related to a laser.
  - `setLaser.m` - laser model initialization.
  - `gaussianPulse.m` - definition of the Gaussian beam.
- `pusher/` - scripts related to electrons.
  - `setElectrons.m` - electron bunch initialization.
  - `electronPusher.m` - electron equations of motion solver.
- `spectrum/` - scripts related to spectra calculation.
  - `calculateSingleSpectra.m` - calculates the spectrum for an observer at a certain position.
  - `calculateFullSpectra.m` - calculates the total spectrum integrated over solid angle.
  - `calculateDivergency.m` - calculate spatial distribution of radiation over solid angle.
  - `scatteredField.m` - calculates radiation field for a given electron.
  - `fourier.m` - calculation and Fourier transform of radiation field of all electrons.
- `plot/` - plotting scripts.
  - `plotLaser.m` - plot the time evolution of a y-component of the laser field.
  - `plotTrajectory.m` - plot the electron trajectory in xy-plane.
  - `plotRadiation.m` - plot the time evolution of a y-component of the radiation field
  - `plotSpectra.m` - plot the single calculated spectrum.
  - `plotAll.m` - plot all above.
- `extension/` - auxiliary packages.

Appendix B

COCO simulation input file

COCO simulation is controlled trough the input file (`inputdeck.m`) (Code. 4.1), which is located in the main folder of the simulation package. In this file, the electron bunch configuration, parameters of a laser, position of the observer and other setting necessary for running the code are defined. User can easily change the default settings and run own simulation.

The input file is separated into 9 sections; each section defines different category of initial parameters. The description of each category, as well as corresponding variables defined within the category is give below the code 4.1.

Code 4.1: *COCO* simulation setup: inputdeck.m

```
%%% Initialization
coco_dir    = '/gpfs/home/tkerepecky/COCO5';
out_dir     = '/home/Toker/Plocha/output/my_gauss';
cd(coco_dir);
addpath(genpath(pwd));
importConstants;

%%%% Parallel computing
num_cores = 16;
numberOfCPU(num_cores);

%%% Laser parameters
a0          = 0.2;
l0          = 800 * nano;
sig0        = 8.5e-06;
FWHM        = 20 * femto;
laser       = 'gauss_gauss';
pn          = 0;
partsOfPi   = 0;
```

```
%%% Electron parameters
el_num      = 1000;
el_en       = 10.22* mev;
el_spread   = 1 * mev;
el_size     = [10 10 0];
el_phi      = 0 * mrad;
el_the      = 0 * mrad;
el_phi_div  = 0 * mrad;
el_the_div  = 0 * mrad;



%%% Time parameters
dt          = 0.01 * femto;
t_start     = -60 * femto ;
t_end       = 60 * femto;

%%% Spectra parameters
exp_en      = 4;

%%% Type of simulation
singleSpectra   = 1;
    n           = [-1 0 0];
    plot_type   = 1;

fullSpectra     = 0;
divergency      = 0;
    div_dist     = 1;
    dangle       = 0.001;
    div_phi      = -0.015:dangle:0.015;
    div_the      = -0.015:dangle:0.015;

%%% Output
fig_visible = 0;
save_img    = 1;
    save_img_type = 'png';

save_work   = 1;
clearall    = 0;

%%% RUN SIMULATION
coco;
```

Section 1 - Initialization

- `coco_dir` - the main folder of $\mathcal{COCO}$ simulation package.
- `out_dir` - the output folder, where a simulation data and images are save.
- `importConstants` - the initialization of physical and simulation constants.

Section 2 - Parallel computing

- `num_cores` - the number of cores used for a parallel computing (0/1 for serial computing).

Section 3 - Laser parameters (Sec.4.1.1).

- `a0` - the laser strength parameter.
- `l0` - the laser wavelength.
- `sig0` - the laser beam waist.
- `FWHM` - the full width at half maximum for Gaussian temporal profile.
- `laser` - the model of a laser (see 4.1.1).
- `pn` - the number of laser phase shifts (not defined for Gaussian beam).
- `partsOfPi` - the laser phase shift pn $\cdot \frac{\pi}{\text{partsOfPi}}$.

Section 4 - Electron parameters (Sec 4.1.2)

- `el_num` - the number of electrons within a bunch.
- `el_en` - the mean energy of an electron bunch.
- `el_spread` - the standard deviation of electron energies in the bunch.
- `el_size` - the size of an electron bunch
- `el_phi` - the electron bunch propagation angle φ_e (see Fig. 4.2).
- `el_the` - the electron bunch propagation angle θ_e.
- `el_phi_div` - the electron bunch divergence $\Delta\varphi_e$.
- `el_the_div` - the electron bunch divergence $\Delta\theta_e$.

Section 5 - Time parameters

- `dt` - the simulation time step.
- `t_start` - the beginning of the simulation.
- `t_end` - the end of the simulation.

Section 6 - Spectra parameters

- `exp_en` - the expected maximum energy in the spectrum (in multiples of a mean energy of the spectrum).

Section 7 - Type of simulation

- `singleSpectra` - calculates the spectrum for an observer at a certain position.

  Following variables are applied only for `singleSpectra` calculation.

  - `n` - the position of the observer.
  - `plot_type` - the type of a generated graph:
    - 1 = 'All four following graphs',
    - 2 = 'Time evolution of a y-component of the laser field',
    - 3 = 'Electron trajectory in xy-plane',
    - 4 = 'Time evolution of a y-component of the radiation field',
    - 5 = 'Calculated spectrum'.
- `fullSpectra` - calculates the total spectrum integrated over solid angle.
- `divergency` - calculate spatial distribution of radiation over solid angle.

  Following variables are applied only for `fullSpectra` or `divergency` calculation.

  - `div_dist` - the distance x of the observer (Fig. 4.4).
  - `dangle` - the numerical angle step for vectors φ_P and θ_P.
  - `div_phi` - the observing angle φ_P (Fig. 4.4).
  - `div_the` - the observing angle θ_P (Fig. 4.4).

Section 8 - Output

- `fig_visible` - if 1 is set, figure is visible.
- `save_img` - if 1 is set, figure is saved in `out_dir` folder.
  - `save_img_type` - format of the saved image ('pdf', 'png', 'eps').
- `save_work` - save simulation data.
  - 1 = save all data (for electron bunch could be extremely large),
  - 2 = save only final data (spectrum, total spectrum, divergence).
- `clearall` - clear all variables after a simulation. This is useful when for-loops are applied in input file in order to run more simulations.

Section 9 - RUN SIMULATION

- `coco` - run the main $\mathcal{COCO}$ simulation script `coco.m`.

Bibliography

[1] NEDOREZOV, Vladimir G.; TURINGE, Andrei A.; SHATUNOV, Yurii M. Photonuclear experiments with Compton-backscattered gamma beams. Physics-Uspekhi, 2004, 47.4: 341.

[2] THIROLF, P. G., et al. Perspectives for photofission studies with highly brilliant, monochromatic gamma-ray beams. In: EPJ Web of Conferences. EDP Sciences, 2012. p. 08001.

[3] TEŞILEANU, Ovidiu, et al. Extreme light infrastructure–nuclear physics. In: Journal of Physics: Conference Series. IOP Publishing, 2013. p. 012157.

[4] WEEKS, K. J.; LITVINENKO, V. N.; MADEY, J. M. J. The Compton backscattering process and radiotherapy. Medical physics, 1997, 24.3: 417-423.

[5] TOMMASINI, R., et al. Development of Compton radiography of inertial confinement fusion implosions a. Physics of Plasmas, 2011, 18.5: 056309.

[6] TOYOKAWA, Hiroyuki, et al. High-energy photon radiography system using laser-Compton scattering for inspection of bulk materials. Review of scientific instruments, 2002, 73.9: 3358-3362.

[7] JOHNSON, Montgomery H.; TELLER, Edward. Intensity changes in the Doppler effect. Proceedings of the National Academy of Sciences, 1982, 79.4: 1340-1340.

[8] SANDORFI, A. M., et al. The fabrication of a very high energy polarized gamma ray beam facility and a program of medium energy physics research at the national synchrotron light source. Brookhaven National Laboratory Report BNL-32717, BNL Physics Department, Proposal to the Department of Energy, 1982.

[9] PHUOC, K. Ta, et al. All-optical Compton gamma-ray source. arXiv preprint arXiv:1301.3973, 2013.

[10] CHEN, S., et al. MeV-energy X rays from inverse Compton scattering with laser-wakefield accelerated electrons. Physical review letters, 2013, 110.15: 155003.

[11] CORDE, Sébastien, et al. Femtosecond x rays from laser-plasma accelerators. Reviews of Modern Physics, 2013, 85.1: 1.

[12] LU, Wei, et al. Generating multi-GeV electron bunches using single stage laser wakefield acceleration in a 3D nonlinear regime. Physical Review Special Topics-Accelerators and Beams, 2007, 10.6: 061301.

[13] AMIRANOFF, F., et al. Observation of laser wakefield acceleration of electrons. Physical Review Letters, 1998, 81.5: 995.

[14] ESAREY, E.; TING, A.; SPRANGLE, P. Laser wakefield acceleration. In: Proceedings of the 1989 IEEE international conference on plasma science (Abstracts). 1989.

[15] ESAREY, E.; SCHROEDER, C. B.; LEEMANS, W. P. Physics of laser-driven plasma-based electron accelerators. Reviews of Modern Physics, 2009, 81.3: 1229.

[16] SARACHIK, E. S.; SCHAPPERT, G. T. Classical theory of the scattering of intense laser radiation by free electrons. Physical Review D, 1970, 1.10: 2738.

[17] GIBBON, Paul. Short pulse laser interactions with matter. World Scientific Publishing Company, 2004.

[18] ESAREY, Eric; RIDE, Sally K.; SPRANGLE, Phillip. Nonlinear Thomson scattering of intense laser pulses from beams and plasmas. Physical Review E, 1993, 48.4: 3003.

[19] KHARIN, V. Yu; SEIPT, Daniel; RYKOVANOV, S. G. Temporal laser-pulse-shape effects in nonlinear Thomson scattering. Physical Review A, 2016, 93.6: 063801.

[20] THOMAS, A. G. R. Algorithm for calculating spectral intensity due to charged particles in arbitrary motion. Physical Review Special Topics-Accelerators and Beams, 2010, 13.2: 020702.

[21] CHEN, M., et al. Modeling classical and quantum radiation from laser-plasma accelerators. Physical Review Special Topics-Accelerators and Beams, 2013, 16.3: 030701.

[22] EPOCH. Extendable PIC Open Collaboration [online]. [Accessed 8 May 2017]. Available from: `http://www.ccpp.ac.uk/codes.html`

[23] AGOSTINELLI, Sea, et al. GEANT4—a simulation toolkit. Nuclear instruments and methods in physics research section A: Accelerators, Spectrometers, Detectors and Associated Equipment, 2003, 506.3: 250-303.

[24] TAJIMA, T.; DAWSON, J. M. Laser electron accelerator. Physical Review Letters, 1979, 43.4: 267.

[25] BAUER, D. Theory of intense laser-matter interaction. Max-Plank-Institute Kernphysik, Heidelberg, Germany, 2006.

[26] LEEMANS, W. P., et al. Multi-GeV electron beams from capillary-discharge-guided subpetawatt laser pulses in the self-trapping regime. Physical review letters, 2014, 113.24: 245002.

[27] WANG, Xiaoming, et al. Quasi-monoenergetic laser-plasma acceleration of electrons to 2 GeV. Nature communications, 2013, 4.

[28] JU, Jinchuan. Electron acceleration and betatron radiation driven by laser wakefield inside dielectric capillary tubes. 2013. PhD Thesis. Université Paris Sud-Paris XI.

[29] Longitudinal mode. Wikipedia [online]. 9 April 2017. [Accessed 8 May 2017]. Available from: https://en.wikipedia.org/wiki/Longitudinal_mode

[30] LAMB JR, Willis E. Theory of an optical maser. Physical Review, 1964, 134.6A: A1429.

[31] STRICKLAND, Donna; MOUROU, Gerard. Compression of amplified chirped optical pulses. Optics communications, 1985, 55.6: 447-449.

[32] RUS, B., et al. ELI-Beamlines laser systems: status and design options. In: SPIE Optics+ Optoelectronics. International Society for Optics and Photonics, 2013. p. 87801T-87801T-12.

[33] HERNANDEZ-GOMEZ, C., et al. The vulcan 10 pw project. In: Journal of Physics: Conference Series. IOP Publishing, 2010. p. 032006.

[34] ZOU, J. P., et al. Design and current progress of the Apollon 10 PW project. High Power Laser Science and Engineering, 2015, 3: e2.

[35] ZHANG, Peng; RIDGERS, C. P.; THOMAS, A. G. R. The effect of nonlinear quantum electrodynamics on relativistic transparency and laser absorption in ultra-relativistic plasmas. New Journal of Physics, 2015, 17.4: 043051.

[36] CHEN, Francis F.; SMITH, Mark D. Plasma. John Wiley and Sons, Inc., 1984.

[37] Plasma (physics). Wikipedia [online]. 28 April 2017. [Accessed 8 May 2017]. Available from: https://en.wikipedia.org/wiki/Plasma_(physics)

[38] LEUCHS, G. Multiphoton ionization of atoms. Laser Physics, 1983, 174-194.

[39] EBERLY, Joseph H.; JAVANAINEN, Juka; RZAŻEWSKI, Kazimierz. Above-threshold ionization. Physics reports, 1991, 204.5: 331-383.

[40] Die Freie Universität Berlin. Interaction of Strong Laser Fields with Matter [online]. 28 April 2017. [Accessed 8 May 2017]. Available from: http://www.diss.fu-berlin.de/diss/servlets/MCRFileNodeServlet/FUDISS_derivate_000000005776/07_Chapter03.pdf?hosts

[41] PUKHOV, Alexancer; MEYER-TER-VEHN, Jürgen. Laser wake field acceleration: the highly non-linear broken-wave regime. Applied Physics B: Lasers and Optics, 2002, 74.4: 355-361.

[42] Krus, Miroslav, 2015, Electron beam acceleration with femtosecond lasers for generationof secondary femtosecond X-ray sources. Dissertation thesis. Czech Technical University in Prague.

[43] ESAREY, E., et al. Electron injection into plasma wakefields by colliding laser pulses. Physical Review Letters, 1997, 79.14: 2682.

[44] BEHM, K. T., et al. Ionization injection effects in x-ray spectra generated by betatron oscillations in a laser wakefield accelerator. Plasma Physics and Controlled Fusion, 2016, 58.5: 055012.

[45] MODENA, A., et al. Electron acceleration from the breaking of relativistic plasma waves. nature, 1995, 377.6550: 606.

[46] GONSALVES, A. J., et al. Tunable laser plasma accelerator based on longitudinal density tailoring. Nature Physics, 2011, 7.11: 862-866.

[47] HANSSON, Martin, et al. Down-ramp injection and independently controlled acceleration of electrons in a tailored laser wakefield accelerator. Physical Review Special Topics-Accelerators and Beams, 2015, 18.7: 071303.

[48] HOOKER, Simon Martin. Developments in laser-driven plasma accelerators. Nature Photonics, 2013, 7.10: 775-782.

[49] LIU, J. S., et al. All-optical cascaded laser wakefield accelerator using ionization-induced injection. Physical review letters, 2011, 107.3: 035001.

[50] CLAYTON, C. E., et al. Self-guided laser wakefield acceleration beyond 1 GeV using ionization-induced injection. Physical Review Letters, 2010, 105.10: 105003.

[51] PAK, Arthur, et al. Injection and trapping of tunnel-ionized electrons into laser-produced wakes. Physical Review Letters, 2010, 104.2: 025003.

[52] FAURE, Jérôme, et al. Controlled injection and acceleration of electrons in plasma wakefields by colliding laser pulses. Nature, 2006, 444.7120: 737.

[53] Relativistic speed. Wikipedia [online]. 4 April 2017. [Accessed 8 May 2017]. Available from: `https://en.wikipedia.org/wiki/Relativistic_speed`

[54] MANGLES, S. P. D. An Overview of Recent Progress in LaserWakefield Acceleration Experiments. CERN Yellow Reports, 2016, 1: 289.

[55] MALKA, Victor, et al. Electron acceleration by a wake field forced by an intense ultrashort laser pulse. Science, 2002, 298.5598: 1596-1600.

[56] GONSALVES, A. J., et al. Generation and pointing stabilization of multi-GeV electron beams from a laser plasma accelerator driven in a pre-formed plasma waveguide a. Physics of Plasmas, 2015, 22.5: 056703.

[57] WANG, Xiaoming, et al. GeV electrons and high brightness betatron x-rays from petawatt-laser-driven plasma accelerators. In: Lasers and Electro-Optics (CLEO), 2014 Conference on. IEEE, 2014. p. 1-2.

[58] HAFZ, Nasr AM, et al. Generation of high-quality electron beams by ionization injection in a single acceleration stage. High Power Laser Science and Engineering, 2016, 4: e24.

[59] ZENG, Ming, et al. Self-truncated ionization injection and consequent monoenergetic electron bunches in laser wakefield acceleration. Physics of Plasmas, 2014, 21.3: 030701.

[60] ZHAO, T. Z., et al. Characterization of electrons and x-rays produced using chirped laser pulses in a laser wakefield accelerator. Plasma Physics and Controlled Fusion, 2016, 58.10: 105003.

[61] SHAW, J. L., et al. Role of direct laser acceleration of electrons in a laser wakefield accelerator with ionization injection. Physical Review Letters, 2017, 118.6: 064801.

[62] WANG, W. T., et al. High-Brightness High-Energy Electron Beams from a Laser Wakefield Accelerator via Energy Chirp Control. Physical Review Letters, 2016, 117.12: 124801.

[63] DÖPP, A., et al. Energy boost in laser wakefield accelerators using sharp density transitions. Physics of Plasmas, 2016, 23.5: 056702.

[64] GUILLAUME, Emilien, et al. Electron rephasing in a laser-wakefield accelerator. Physical review letters, 2015, 115.15: 155002.

[65] BOHACEK, K., et al. Generation of laser-driven femtosecond electron beams for secondary photon sources with 7 TW Ti-sapphire laser system at PALS.

[66] HELL. ELI Beamlines [online]. 4 April 2017. [Accessed 8 May 2017]. Available from: `https://www.sif.it/static/SIF/resources/public/files/congr14/ip/Levato.pdf`

[67] Hirayama. Photon interactions and Cross Sections [online]. 4 April 2017. [Accessed 8 May 2017]. Available from: `http://rcwww.kek.jp/research/shield/photon_r.pdf`

[68] A. H. Compton, "A quantum theory of the scattering of x-rays by light elements," Physical review, vol. 21, no. 5, p. 483, 1923.

[69] CHEN, J. G., et al. The Proto Type of Shanghai Laser Electron Gamma Source at 100 MeV LINAC. arXiv preprint nucl-ex/0610042, 2006.

[70] PHUOC, K. Ta, et al. All-optical Compton gamma-ray source. arXiv preprint arXiv:1301.3973, 2013.

[71] A. HIROSE, *Radiation by Moving Charges*. University of Saskatchewan.

[72] JACKSON, John David; FOX, Ronald F. Classical electrodynamics. American Journal of Physics, 1999, 67.9: 841-842.

[73] RILEY, K. F.; HOBSON, M. P.; BENCE, S. J. Mathematical methods for physics and engineering. 1999.

[74] CORDE, Sébastien, et al. Femtosecond x rays from laser-plasma accelerators. Reviews of Modern Physics, 2013, 85.1: 1.

[75] Relativistic mechanics. Wikipedia [online]. 17 February 2017. [Accessed 8 May 2017]. Available from: `https://en.wikipedia.org/wiki/Relativistic_mechanics#Force`

[76] REVILLE, Brian; KIRK, John G. Computation of synthetic spectra from simulations of relativistic shocks. The Astrophysical Journal, 2010, 724.2: 1283.

[77] SPIEGEL, Murray R. Advanced mathematics. McGraw-Hill, Incorporated, 1991.

[78] OSIRIS. PICKSC [online]. [Accessed 8 May 2017]. Available from: http://picksc.idre.ucla.edu/software/software-production-codes/osiris/

[79] WANG, Zhongyang, et al. Space-time profiles of an ultrashort pulsed Gaussian beam. IEEE journal of quantum electronics, 1997, 33.4: 566-573.

[80] Nyquist–Shannon sampling theorem. Wikipedia [online]. 8 May 2017. [Accessed 8 May 2017]. Available from: https://en.wikipedia.org/wiki/Nyquist%E2%80%93Shannon_sampling_theorem